Infrared Emission of Normal Galaxies from 2.5 to 12 Microns: *ISO* Spectra, Near-Infrared Continuum and Mid-Infrared Emission Features[1]

Nanyao Lu[2], George Helou[2], Michael W. Werner[3], Harriet L. Dinerstein[4], Daniel A. Dale[2,5], Nancy A. Silbermann[2], Sangeeta Malhotra[2,6], Charles A. Beichman[3], Thomas H. Jarrett[2]

ABSTRACT

[2]Infrared Processing and Analysis Center, MS 100-22, California Institute of Technology, Pasadena, CA 91125; lu@ipac.caltech.edu, gxh@ipac.caltech.edu, nancys@ipac.caltech.edu, jarrett@ipac.caltech.edu

[3]Jet Propulsion Laboratory, MS 233-303, 4800 Oak Grove Road, Pasadena, CA 91109; mwerner@sirtfweb.jpl.nasa.gov, chas@mail1.jpl.nasa.gov

[4]Astronomy Department, The University of Texas at Austin, 1 University Station C1400, Austin, TX 78712-0259; harriet@astro.as.utexas.edu

[5]Dept. of Physics and Astronomy, University of Wyoming, Laramie, WY 82071; ddale@uwyo.edu

[6]Dept. of Physics and Astronomy, Johns Hopkins Univ., Baltimore, MD 21218; san@tarkus.pha.jhu.edu

We present ISO-PHOT spectra of the regions 2.5–4.9 μm and 5.8–11.6 μm for a sample of 45 disk galaxies from the U.S. *ISO* Key Project on Normal Galaxies. The galaxies were selected to span the range in global properties of normal, star-forming disk galaxies in the local universe. The spectra can be decomposed into three spectral components: (1) continuum emission from stellar photospheres, which dominates the near-infrared (2.5–4.9 μm; NIR) spectral region; (2) a weak NIR excess continuum, which has a color temperature of $\sim 10^3$ K, carries a luminosity of a few percent of the total far-infrared dust luminosity $L_{\rm FIR}$, and most likely arises from the ISM; and (3) the well-known broad emission features at 6.2, 7.7, 8.6 and 11.3 μm, which are generally attributed to aromatic carbon particles. These aromatic features in emission (AFEs) dominate the mid-infrared (5.8–11.6 μm; MIR) part of the spectrum, and resemble the so-called Type-A spectra observed in many non-stellar sources and the diffuse ISM in our own Galaxy. The few notable exceptions include NGC 4418, where a dust continuum replaces the AFEs in MIR, and NGC 1569, where the AFEs are weak and the strongest emission feature is [S IV] 10.51 μm.

The relative strengths of the AFEs vary by 15–25% among the galaxies. However, little correlation is seen between these variations and either *IRAS* 60 μm-to-100 μm flux density ratio $R(60/100)$ or the far-infrared-to-blue luminosity ratio $L_{\rm FIR}/L_{\rm B}$, two widely used indicators of the current star-formation activity, suggesting that the observed variations are not a consequence of the radiation field differences among the galaxies. We demonstrate that the NIR excess continuum and AFE emission are correlated, suggesting that they are produced by similar mechanisms and similar (or the same) material. On the other hand, as the current star-formation activity increases, the overall strengths of the AFEs and the NIR excess continuum drop significantly with respect to that of the far-infrared emission from large dust grains. In particular, the summed luminosity of the AFEs falls from $\sim 0.2\,L_{\rm FIR}$ for the most "IR-quiescent" galaxies to $\sim 0.1\,L_{\rm FIR}$ for the most "IR-active" galaxies. This is likely a consequence of the preferential destruction in intense radiation fields of the small carriers responsible for the NIR/AFE emission.

Subject headings: galaxies: ISM — infrared: galaxies — infrared: ISM: continuum — infrared: ISM: lines and bands — infrared: dust

---

[1]Based on observations with *ISO*, an ESA project with instruments funded by ESA member states (especially the PI countries: France, Germany, the Netherlands, and the United Kingdom) and with the participation of ISAS and NASA.

1. Introduction

The spectroscopic properties of galaxies in the wavelength range 2.5–12 μm are much less well known than in the optical regime, where stellar emission dominates, and in the far-infrared, where thermal continuum emission from cool interstellar dust dominates. Prior to the *Infrared Space Observatory* (*ISO*; Kessler et al. 1996) mission, spectroscopic information on this wavelength region was available for only a few of the brightest galaxies and galaxy nuclei, which were observed with ground-based telescopes through a few spectral windows (e.g., Roche et al. 1991), or with the *IRAS* Low-Resolution Spectrometer (e.g., Cohen & Volk 1989). However, this relatively unexplored spectral region contains important signatures of interstellar dust particles, in particular the broad emission features at 3.3, 6.2, 7.7, 8.6, and 11.3 μm (Gillett et al. 1973) which in the past were often called the "Unidentified Infrared" or UIR features. These features are now known to be ubiquitous in the ISM of our Galaxy: they are seen in H II and PDR regions (e.g., Césarsky et al. 1996; Roelfsema et al. 1996; Verstraete et al. 1996, 2001); planetary nebulae and circumstellar regions (e.g., Beintema et al. 1996); reflection nebulae (e.g., Boulanger et al. 1996, Uchida, Sellgren, & Werner 1998); and diffuse cirrus clouds (e.g., Mattila et al. 1996; Lemke et al. 1998; Chan et al. 2001). Taken together, they radiate a significant fraction of the total IR emission from these regions (e.g., Puget & Léger 1989).

While the exact identity of the carriers of the UIR features is still unresolved, it is generally agreed that the features arise from vibrational modes of a carbon-based, aromatic material, so we will refer to them hereafter as aromatic features in emission, or "AFEs." Possible candidate materials range from Polycyclic Aromatic Hydrocarbon molecules (hereafter PAHs; Léger & Puget 1984; Allamandola, Tielens, & Barker 1985, 1989; Puget & Léger 1989) to Hydrogenated Amorphous Carbon grains (Duley & Williams 1981, 1988). The current picture is that the particles responsible for the emission, whether present as free molecules or being attached to larger grains, are transiently heated by the absorption of single UV photons to $T \sim 10^3$ K. The carriers of the AFEs may also play an important role in regulating the physical conditions in the ISM by contributing significantly to photoelectric heating of the gas (Bakes & Tielens 1994; Helou et al. 2001; however, for an alternate point of view, see Chan et al. 2001).

The spectral region also hosts a possible near-infrared, non-stellar continuum emission with a color temperature of $\sim 10^3$ K, which was first detected in Galactic reflection nebulae (Andriesse 1978; Sellgren, Werner, & Dinerstein 1983; Sellgren 1984). Recent observations with *COBE* and *IRTS* hint that this near-IR continuum may also be present on larger scales in our Galaxy (Bernard et al. 1994; Tanaka et al. 1996), but it has not been previously reported in external galaxies.

With its unprecedented sensitivity and contiguous wavelength coverage, *ISO* made it possible to obtain 2.5–11.6 μm spectra of large numbers of galaxies that were too faint to observe previously. As part of an *ISO* Key Project to study the physical properties of the ISM in galaxies (Helou et al. 1997; Dale et al. 2000), we obtained 2.5–11.6 μm spectra using the PHT-S mode of ISO-PHOT (Lemke et al. 1996) for 45 galaxies. This survey covered the full range of morphological types of disk galaxies, S0 to Im, that are powered by star formation. Similar *ISO* spectra of other types of galaxies can be found elsewhere: e.g., AGNs (Clavel et al. 2000), ultraluminous IR galaxies (Genzel et al. 1998; Rigopoulou et al. 1999), and galaxies of moderately low surface brightnesses such as the Magellanic Clouds (Reach et al. 2000; Sturm et al. 2000; Vermeij et al. 2002). The AFEs are seen in the spectra of most of these objects, but are absent or too weak to detect in elliptical galaxies (Lu & Hur 2000; 2003; Athey et al. 2002) and extremely metal deficient dwarfs (e.g., Thuan, Sauvage, & Madden 1999).

In Paper I (Helou et al. 2000), we presented spectra for a subsample of 7 galaxies, highlighted the detections of the AFEs and a near-infrared, non-stellar continuum emission, and suggested that the averaged spectrum of a number of galaxies could provide a useful template for redshift determinations of distant star-forming galaxies. In the present paper, we explore more fully the diversity of the 2.5–12 μm spectra of the galaxies in our sample. We present and compare the individual spectra of all the 45 observed galaxies, provide a quantitative analysis of various spectral components, evaluate variations from galaxy to galaxy and possible statistical correlations with galaxy properties at other wavelengths, and discuss possible reasons for these trends. Throughout this paper, we use NIR and MIR to refer to the 2.5–4.9 μm and 5.8–11.6 μm spectral regions respectively, and AFE(3.3), AFE(6.2), AFE(7.7), AFE(8.6) and AFE(11.3) for the corresponding individual features.

2. Galaxy Sample, Observations and Results

2.1. The Sample

The galaxies studied in this paper are a subset of a larger sample observed for the Key Project. This parent sample consists of 69 "normal" galaxies selected to capture the great diversity in the properties of galaxies in the local universe, especially in terms of the ratio of current to past star-formation rate. For each galaxy in this project we obtained at least one of the following: ISO-CAM images at 7 and 15 μm (see Dale et al. 2000), a sparsely sampled ISO-LWS spectrum between 43 and 200 μm targeting fine-structure lines (Malhotra et al. 2001 and references therein), and a PHT-S 2.5–11.6 μm spectrum as presented here.

Table 1 lists the 45 Key Project galaxies for which we obtained a PHT-S spectrum. The position of each observation in the table was reconstructed from the *ISO* pointing history (IIPH) file, which in most cases was the same as the intended position. Nearly all of the observations were taken at the galaxy optical center, except for two off-center positions in NGC 1569 which correspond to emission peaks on the CAM images (Hunter et al. 2001). From Table 1 it can be seen that the blue luminosity L_B ranges from 2×10^9 to $7 \times 10^{10}\, L_\odot$, the FIR-to-blue luminosity ratio $L_{\rm FIR}/L_{\rm B}$ from 0.2 to 15, and the *IRAS* 60-to-100 μm color index $R(60/100)$ from 0.3 to 1.3. The heliocentric velocities [Col. (10)] were used to shift all spectra to a common (rest) frame for easier comparison. The median velocity of the sample is about 1800 km s^{-1}.

Fig. 1 shows the distribution of the galaxies in a plot of $\log L_{\rm FIR}/L_{\rm B}$ *vs.* $R(60/100)$. Most of the galaxies fall along a rough diagonal from the lower left to upper right corner of the diagram, a trend which we attribute to an increasing ratio of present-day star forming activity to the time-averaged star-formation rate in the past (e.g., Helou 1986). In this paper we assume that both axes in Fig. 1 are statistically valid measures of the global amount of current star-formation activity in a galaxy, and thus of the UV-to-optical spectral shape of the radiation field. We define three galaxy subsamples: an "FIR-quiescent" subsample, represented by open squares in Fig. 1; an "FIR-active" group, represented by filled squares; and an intermediate subsample, shown as crosses. The few outliers in Fig. 1 include the compact galaxy NGC 4418, which has higher $R(60/100)$ than 99% of the galaxies in the *IRAS* Bright Galaxy Sample (Soifer et al. 1989), and the low-metallicity irregular galaxy NGC 1569 which has low $L_{\rm FIR}/L_{\rm B}$. Most of the outliers also show peculiarities in their PHT-S spectra; we comment on these individually in §3.2.

2.2. Observations and Data Reduction

The PHT-S spectrometer has two 64-element linear Si:Ga detector arrays. The SS array covers the wavelength range 2.5–4.9 μm with spectral resolution element 0.04 μm while the SL array covers the interval 5.8–11.6 μm with a resolution element of 0.1 μm. The instrument has a $24'' \times 24''$ aperture on the sky, pointed with an accuracy $\leq 2''$ (Kessler et al. 1996). For each galaxy, the SS and SL spectra were obtained simultaneously, through an aperture placed at the position given in Table 1. Sky reference observations were taken at symmetrically placed offsets of $\pm\, 150''$ from the galaxy center along a direction determined by the spacecraft roll angle at the time of the observation. Integration times were 512 seconds, split evenly between the galaxy and sky positions, with a duration of 64 sec per chopper step, except for the faint object IC 860, for which we increased the total integration time to 2048 seconds.

The spectra were derived from the Edited Raw Data using standard procedures in the PHOT Interactive Analysis package (PIA version 7; Gabriel et al. 1997), including deglitching at both ramp and signal levels, ramp slope fitting, signal averaging per chopper position, and sky subtraction of the average signal for the two sky reference positions. The flux calibration was performed using a signal-dependent "detector response function" obtained from chopped observations of calibration stars with known SED's. This "direct calibration," which was later incorporated into pipeline version 8.4, included an empirical correction for the signal loss due to a detector transient induced by the chopper switching between the source and the reference positions.

Since we used point-source flux standards, our spectra represent the effective emission corresponding to the integration of a normalized PHT-S beam profile over the surface brightness distribution of the source, divided by f_{psf}, the fraction of the point-source spread function within the PHT-S aperture (see Appendix A). For the SS detector pixels, the median flux uncertainty $\sigma_{SS}^{median} \sim 25\,\mathrm{mJy}$ and depends only weakly on the source flux. In contrast, σ_{SL}^{median} varies from 15 mJy to 45 mJy over the sample and scales roughly linearly with source brightness. According to the data validation report from pipeline version 8.4, the absolute and relative flux uncertainties are on order of 10% for point sources. As described in Appendix A, we performed an independent check on the flux calibration by comparing our PHT-S data with the CAM imaging data of Dale et al. (2000); these agree to better than 18% for 5–8.5 μm and $\leq 25\%$ for the 4–5 μm region.

2.3. Near-Infrared Photometry

We used near-infrared images from the Large Galaxy Atlas of the 2-Micron All Sky Survey, 2MASS (Jarrett et al. 2003) to derive integrated J (1.25 μm), H (1.65 μm), and Ks (2.17 μm) magnitudes for each galaxy, appropriate to the placement of the PHT-S aperture on the sky during the *ISO* observations. Since there is not yet a finalized conversion formula from the 2MASS magnitude scale to flux densities, we normalized our 2MASS magnitudes to the multi-aperture observations of four early-type galaxies (NGC 4374, NGC 3379, NGC 5866, and NGC 1326) published by Frogel et al. (1978) and Persson, Frogel, & Aaronson (1979), using the magnitude-to-flux conversions of Wilson, Schwartz, & Neugebauer (1972). To adjust our 2MASS photometry to the magnitude scale in these references, we found it necessary to add the following offsets: $(0.028 \pm 0.009)^m$ at J, $(0.052 \pm 0.004)^m$ for H, and $(0.079 \pm 0.010)^m$ to convert from K_s to K (2.2 μm). The resulting 2MASS fluxes are used to normalize our PHT-S spectra in §3 and §4 to unveil the NIR excess continuum in disk galaxies. This requires no significant zero-point offset between the 2MASS and PHT-S flux

scales. We show in Appendix B that this is indeed the case.

2.4. Results

The sky-subtracted, rest-frame PHT-S spectra are presented in Figures 2*a*-2*e*. Table 2 summarizes the PHT-S aperture coverage factor p (see Appendix A), the mean continuum flux density at 4 μm, and a mean flux density for each of the AFEs. These mean flux densities, defined in the footnotes to Table 2, are derived after shifting the spectrum to the rest frame and resampling the data at the PHT-S detector wavelengths by a linear interpolation between the two nearest data points. Note that the mean flux density for AFE(11.3) is basically taken over only the blue side of the feature, since part of the red side fell outside our wavelength coverage. The last 2 lines in Table 2 provide information on two elliptical galaxies, NGC 3379 and NGC 4374, whose PHT-S spectra were discussed by Lu & Hur (2000; 2003), and which served as comparison objects for the disk galaxies (§4.1).

3. The Spectra

3.1. General Characteristics

The great majority of the observed galaxies show qualitatively similar PHT-S spectra. The MIR part of the spectra is typically dominated by the prominent AFE features at 6.2, 7.7, 8.6, and 11.3 μm, which have relative strengths and profiles similar to those of "Type A" Galactic sources as described, for example, by Geballe (1997) and Tokunaga (1997). These features are superposed on a NIR continuum dominated by the emission from stellar photospheres. Of all the spectra, only that of NGC 4418 display MIR structures that are qualitatively different from a Type A spectrum. We discuss in more detail this unique spectrum and a few others in §3.2.

The similarity of most of the spectra in the range 5.8–11.6 μm suggests that it is useful to derive an averaged spectrum to serve as a template for normal, star-forming galaxies. We derived such an average spectrum from 40 of the 45 galaxies in this study, omitting only the atypical galaxies NGC 4418 and NGC 1569 (see above, and §3.2), and the three galaxies with the lowest S/N ratios in their spectra (NGC 3705, NGC 4519, and NGC 7418). The average spectrum was obtained on a wavelength pixel-by-pixel basis from the resampled, rest-frame individual spectra (see §2.4) normalized at some fiducial wavelength. No correction for redshift was made to the *JHK* points described in §2.3, since the effects are negligible for these broad photometric bands.

The averaged spectra resulting from two choices of the fiducial wavelength for normalization are shown in Fig. 3. The open squares depict the spectrum obtained by normalizing the individual spectra at J, while the thick solid curve corresponds to normalizing by the integrated flux of AFE(7.7). In both cases we used $1/\sigma^2$-weighted averaging, where σ is either σ_{SS}^{median} or σ_{SL}^{median} depending on which detector array segment the pixel under consideration belongs to; the *JHK* data points were averaged using the same σ-weights as used for the PHT-SS data.

The error bars in Fig. 3 represent $s/\sqrt{n}$, where s is the standard deviation of the normalized fluxes and n is the number of galaxies included in the average (due to the redshifts of individual galaxies, $n < 40$ for some points near the array edges). For a given pixel, s is given by

$$s^2 = (\Sigma\, w_i f_i^2 - < f >^2 \Sigma\, w_i)/(\frac{n-1}{n}\Sigma\, w_i), \tag{1}$$

where f_i and w_i are respectively the flux density and weight from the ith sample galaxy, and $< f >$ is the average flux of the pixel. Therefore, these error bars reflect mainly the variation of spectral shape within the sample. Note that the two normalization methods have different biases: normalization at $7.7\,\mu$m gives greater weight to individual spectra which are more dominated by emission from the ISM (e.g., the AFEs), whereas normalization at J gives greater weight to galaxies with a larger proportional contribution of starlight.

The averaged spectra in Fig. 3 can be compared with the "template" spectrum presented in Fig. 2 of Paper I. The latter was a straight average [i.e., with $w_i \equiv 1$ in eq. (1)] over a subset of 28 galaxies. In addition, a different PHOT calibration and a different normalization parameter (the strength of the $6.2\,\mu$m AFE) was used. The main differences are limited to $\lambda < 3\,\mu$m; the MIR region of the template spectrum from Paper I is very similar to those derived here if they are all normalized in the same way.

We also compare our average disk galaxy spectra with those of the two elliptical galaxies, NGC 3379 and NGC 4374. The PHT-S spectra of these two E1 galaxies, reduced from the *ISO* archive data by Lu & Hur (2003), are shown in Fig. 3 as a thin solid line and dotted line respectively. At a heliocentric redshift of $v_h = 911\,\mathrm{km\ s^{-1}}$, NGC 3379 (M 105) is one of the nearest normal giant elliptical galaxies, with a classical $\mathrm{r}^{\frac{1}{4}}$ profile (de Vaucouleurs & Capaccioli 1979). NGC 4374 (M 84), at $v_h = 1060\,\mathrm{km\ s^{-1}}$, is known to host a central radio source (cf. Bridle & Perley 1984), and contains at least some interstellar matter, indicated by the presence of dust lanes and *IRAS* detections at 60 and $100\,\mu$m. Nevertheless, these two ellipticals have quite similar PHT-S spectra, nearly featureless and falling roughly as a Rayleigh-Jeans law from 1.25 to $\sim 7\,\mu$m. An apparent flattening beyond $8\,\mu$m may be due to circumstellar dust emission (Knapp, Gunn, & Wynn-Williams 1992; Athey et al. 2002).

It can be seen from Fig. 3 that the spiral galaxies show clear excess emission compared to the ellipticals at all wavelengths $\geq 2.2\,\mu$m. In Table 3, we list the numerical values of the two average disk-galaxy spectra in Fig. 3, as well as the average for the two E galaxies. These averaged spectra, because of their high S/N, offer a more sensitive way to study the profiles of the brighter AFEs and to look for weak features that might be buried in noise in individual spectra.

Table 4 summarizes the features that are identifiable in the averaged spectra in Fig. 3 and were discussed in Paper I. The equivalent widths of some of weaker features were estimated on the AFE(7.7)-normalized spectrum and are given in the last column of Table 4. The $3.3\,\mu$m feature, which is not apparent in most of the individual galaxy spectra, is easily recognized in the averaged spectrum, and the narrow feature at around $4.03\,\mu$m is probably H I Brα. The hump near $7.0\,\mu$m could be either [Ar II] $6.99\,\mu$m and/or the $6.9\,\mu$m dust feature discussed by Bregman et al. (1983) and Cohen et al. (1986), with possibly a small contribution from H_2 $6.910\,\mu$m v=0–0 S(5). The small bump at around $10.6\,\mu$m could arise from [S IV], which is seen most distinctly in the post-starburst galaxy NGC 1569. Finally, the asymmetric appearance of AFE(7.7) is probably a result of the blending of two unresolved peaks at 7.6 and $7.8\,\mu$m; such substructure has been seen in some Galactic sources (e.g., Bregman 1989; Roelfsema et al. 1996), and is partially resolved in some of the highest-S/N spectra in this study (e.g. NGC 4194 and IC 883, see Fig. 2).

In order to assess whether the the MIR spectral shape varies with star-formation activity, we compared the average spectra for the FIR-quiescent and FIR-active subsamples defined in §2.1, which include 14 galaxies each. The average spectra for the J-band normalization described above, aligned at J for comparison, are shown in Fig. 4*a* as the solid curve (FIR-quiescent) and open squares (FIR-active). It can be seen from the figure that both the NIR continuum and AFEs for the FIR-active galaxies lie well above those of the FIR-quiescent subsample. On the other hand, when the averages are normalized by AFE(7.7) and aligned at $7.7\,\mu$m (Fig. 4*b*), the FIR-quiescent spectrum lies above the FIR-active one only in the NIR region. (The small difference between the two spectra in Fig. 4*b* in the region 9–10 μm is significant only at the $1.5\,\sigma$ level.) Note that the apparent "dips" around 3.2, 3.7 and $4.1\,\mu$m seen in Fig. 4*b* are probably not real, but are due to the AFE(7.7) normalization, which yields an overly strong weighting for the (noisy, and in some cases negative) short-wavelength data points of galaxies with strong AFEs and faint NIR continua.

These plots demonstrate that the only significant spectral difference between the two subsamples lies in the NIR, and can be attributed to different contributions from starlight. In other words, the spectral shape of the MIR AFEs in galaxies remains largely independent of star-formation activity.

3.2. Remarks on Individual Spectra

3.2.1. NGC 520

NGC 520 (Arp 157), classified as an intermediate-stage merger by Hibbard & van Gorkom (1996), is as radio- and infrared-bright as NGC 4038/4029 (Arp 244; the Antennae). Numerical simulations suggest that NGC 520 is a merger remnant resulting from two disk galaxies which began colliding about 300 million years ago (Stanford & Balcells 1991). Our PHT-S aperture was placed on the main optical ridge, $\sim 14''$ north of the emission peak in the 10 μm image of Bushouse, Telesco, & Werner (1998). This peak is presumably the dust-obscured nucleus of the brighter galaxy in the pair (see Fig. 6 of Stanford & Balcells 1990). The PHT-S spectrum therefore included both this obscured nucleus and parts of the disks of both galaxies.

The most striking aspect of the spectrum of NGC 520 is the weakness of AFE(8.6) and AFE(11.3) relative to AFE(7.7). On the other hand, AFE(6.2) has normal (Type A) strength relative to AFE(7.7). In the context of the PAH model, both AFE(8.6) and AFE(11.3) arise primarily from C-H bending modes, while AFE(6.2) and AFE(7.7) come from C-C modes. Thus, a plausible conjecture is that the compression of the ISM due to the interaction of the merging galaxy disks might have led to a high degree of dehydrogenation of PAHs, resulting in relatively weak 8.6 and 11.3 μm features.

3.2.2. NGC 1569

NGC 1569 is a nearby Magellanic-type irregular galaxy with a metallicity $\sim 30\%$ of solar. It experienced a strong burst of star formation as recently as a few million years ago (Israel 1988; Israel & van Driel 1990; Greggio et al. 1998). We obtained PHT-S spectra at three positions on the galaxy disk. Position C (see Table 1) is on the nucleus, which also hosts one of the two superluminous young star clusters in this galaxy, Cluster B (Ables 1971; Arp & Sandage 1985). Positions NW and SE are located ($16\farcs0$ W, $5''$ N) and ($16\farcs6$ E, $7''$ S) of the nucleus respectively. These correspond respectively to the NW and SE peaks on our CAM LW2 image (Hunter et al. 2001) as well as to H II regions No. 2 and No. 7 in Table 3 of Waller (1991).

All three spectra show a strong, unresolved emission line at 10.55 ($\pm$0.05) μm, which presumably is [S IV] 10.51 μm. We may also have detected [Ar III] 8.99 μm, in the NW and SE spectra. If present, it is a factor of 5–10 weaker than [S IV] 10.51 μm, indicating a relatively high effective temperature for the illuminating radiation field (e.g., Rank et

al. 1978; Rubin 1985). This is consistent with the conclusions of Hunter et al. (2001), who infer T_{eff} = 40,000 K based on the Key Project LWS spectroscopy and other data. The large inferred number of early-type O stars indicates recent vigorous star-formation activity in NGC 1569 (Hunter et al. 2001).

The unusual strength of the ionic lines relative to the dust emission in NGC 1569 carries over to longer wavelengths. Its value of L([O III] 88 μm)/$L_{\rm FIR}$, where L([O III] is the luminosity in the [O III] 88 μm line emission, is higher by an order of magnitude or more (1.0–1.5 dex) than that of nearly all of the other galaxies in the Key Project sample (see Fig. 6*a* of Malhotra et al. 2001). The only other galaxy with such high-contrast ionic line emission is IC 4662, for which, unfortunately, we did not obtain a PHT-S spectrum. Recall also that NGC 1569 was an outlier in Fig. 1, having unusually low $L_{\rm FIR}/L_{\rm B}$ for its *IRAS* color index $R(60/100)$. Whether this is due to the recent starburst or is a consequence of low metallicity is unclear, but the weak dust compared to the gas emission suggests a low dust-to-gas ratio in NGC 1569, and therefore possibly a high mean free path for far-UV photons as well as a hard UV radiation field.

3.2.3. NGC 4418

The PHT-S spectrum of NGC 4418 is markedly different from those of nearly all the other sample galaxies: the AFEs are not seen, and the MIR spectrum is dominated by an apparent emission plateau extending from 6–9 μm, which has been interpreted as arising from a broad continuum upon which is superposed a deep 10 μm silicate absorption feature (Roche et al. 1986).

NGC 4418 was previously noticed to be an extreme object by Malhotra et al. (1997), who pointed out its extreme deficiency in the [C II] 157 μm line. It is a good example of the now well-established trend, that L([C II] 157 μm)/$L_{\rm FIR}$ to $L_{\rm FIR}$ decreases as the FIR luminosity and intensity of the dust-heating radiation field increases (Malhotra et al. 1997; Luhman et al. 1998). The nature of the illuminating radiation field in NGC 4418 is unclear, although its FIR color index, $R(60/100) = 1.3$, is the highest ("warmest") in the full Key Project sample (see Table 5 of Malhotra et al. 2001). NGC 4418 is a very compact source at radio wavelengths, with a radius of $\leq 0\farcs5$ ($\sim 53h^{-1}$ pc) at 20 cm (Condon et al. 1990), so our PHT-S spectrum enclosed most (84%) of its MIR emission. On the one hand, our PHT-S spectrum of NGC 4418 resembles the *ISO* spectrum of an ultra-compact H II region in M17 (Césarsky et al. 1996), which would be consistent with the suggestion that NGC 4418 contains an intense nuclear starburst of very high optical depth. On the other hand, Spoon et al. (2001) report seeing absorption features from ices in the PHT-S spectrum, and interpret

NGC 4418 as a dust- and ice-enshrouded active galactic nucleus (AGN).

3.2.4. IC 860

IC 860 is also compact, with a 20 cm diameter of $< 0\farcs4$ (or $100h^{-1}$pc; Condon et al. 1990), consequently, our PHT-S aperture included about 81% of its MIR emission. This galaxy has been generally classified as a non-AGN (e.g., Leech et al. 1989). Given its compact size, warm FIR color of $R(60/100) = 0.94$, and high value of $\log L_{\rm FIR}/L_{\rm B} = 1.05$, it is plausible that IC 860 harbors a nuclear starburst. While the AFEs in IC 860 have typical relative strengths, they have a low collective intensity relative to the FIR dust emission (see §4.3). IC 860 was also one of the extremely "[C II]-deficient" galaxies noted by Malhotra et al. (1997). If the carriers of the AFEs are major contributors of photoelectrons that heat the gas, these two observations taken together are consistent with the destruction of a substantial fraction of the AFE carriers by an intense UV radiation field.

3.2.5. NGC 5866

NGC 5866 is a nearby, early-type (S0), edge-on disk galaxy, with a dust lane visible in optical and the "coolest" FIR color index in the entire Key Project sample, $R(60/100) = 0.3$ The CAM LW2 image (Malhotra et al. 2000) shows that the emission at 7 μm arises mainly from the edge-on disk of the galaxy. Our PHT-S aperture was centered roughly on the nucleus, and enclosed about 60% of the total flux of the galaxy.

The PHT-S spectrum of NGC 5866 shows a strong continuum rising towards shorter wavelengths, consistent with the picture that the global emission from this galaxy is strongly dominated by stellar photospheric emission. There appears to be a broad emission feature that peaks at 7.9 μm, instead of the usual AFE(7.7 μm) feature. The 8.6 μm feature is weak, if present, and the 11.3 μm feature is much wider than usual. Taken together, these AFEs are unusually weak relative to the FIR dust emission as compared to the other FIR-quiescent galaxies in the sample (see §4.3 below).

4. Analysis and Discussion

4.1. Continuum Emission at 3 to 5 Microns

Spectral synthesis models indicate that as long as the luminosity of a galaxy is dominated by relatively old stellar populations (i.e., older than a few Gyrs), the shape of its stellar continuum spectrum in near-infrared remains largely independent of the details of its star formation history (e.g., Bruzual & Charlot 1993). This is supported by results from 2MASS, which show that normal galaxies display a much smaller color dispersion in the near-infrared than in the optical (e.g., Jarrett 2000). We therefore assume that the averaged elliptical galaxy spectrum (§3.1) is representative of the intrinsic spectral shape of the stellar component in our disk galaxies. It is uncertain whether the circumstellar dust emission longward of 8 μm can also be scaled in this way, but for disk galaxies, the emission is much fainter than the ISM emission in this spectral region.

We first investigated whether internal reddening by dust can account for the observed NIR excess emission. In Fig. 5, the same 40 galaxies[7] included in the average spectrum (see §3.1) are shown in two color-color plots: logarithmic flux-density ratios K/J *vs.* H/J, and f(4 μm)/J *vs.* H/J, respectively. The galaxies are coded according to their degree of FIR-activity in the same way as in Fig. 1, and the elliptical galaxies are shown as open circles. We considered two geometries for the dust extinction: a foreground dust screen (shown as solid lines in Fig. 5); and the case of uniformly mixed stars and dust (shown as dotted curves). In both cases, we used a near-infrared reddening law of $A(\lambda)/A(J) = (\lambda/1.25\mu\mathrm{m})^{-1.7}$, after Mathis (1990). We assumed zero reddening for the ellipticals. The tick marks indicate A_V = 1, 2, and 3^m respectively, for the dust screen model; in the star/dust mixed case, one requires about 3 times as much total dust column density in order to produce the same amount of reddening as for the foreground screen. Apart from this scale factor, the two cases produce very similar trends in Fig. 5 within the parameter space occupied by our galaxies. As one can see from the figure, most of the galaxies lie above the reddening lines, particularly in the lower panel, f(4 μm)/J *vs.* H/J. Therefore, it appears that dust reddening cannot account for the color differences between our sample of disk galaxies and the reference elliptical galaxies. There must be an additional continuum component which becomes more prominent at the longer wavelengths.

We set out to reconstruct the character of this "NIR excess continuum" as follows. We

[7]In §4 we use galaxies drawn from this 40-galaxy sample only. In comparing PHT-S fluxes with the FIR fluxes (i.e., in Tables 5 and 7, and Fig. 9), we further exclude those few without a PHT-S aperture coverage factor p in Table 2.

assumed that the J and H emission in the disk galaxies arises only from stars. Next, we subtracted the averaged elliptical galaxy spectrum in Table 3 from the data for each disk galaxy, after reddening it to the H/J color of the latter using the foreground screen case. (For the few cases where the observed H/J color is slightly bluer than that of the ellipticals, we take $A_V = 0$.) Finally, to increase the S/N ratio, we averaged the residual spectra for the entire galaxy sample. The result is shown in Fig. 6*a*. Also shown is a modified black-body curve for $T = 750\,\mathrm{K}$ and a λ^{-2} emissivity law, which fits the general shape of the curve quite well. The emission is clearly much broader and stronger than AFE($3.3\,\mu$m), and therefore is unlikely to be simply the wings of this feature.

The residual spectrum shown in Fig. 6*a* represents a lower limit to the typical intensity of this NIR excess continuum, because of our assumption that it does not contribute at H. In order to set an upper limit to such a contribution, we considered the effects of assuming that only the J-band flux has no contribution from non-stellar sources, and derived the residual spectrum that results from subtracting the elliptical galaxy spectrum uncorrected for different reddening between the disk and E galaxies. This yields the average residual spectrum shown in Fig. 6*b*, which is well fit by a modified black-body curve with $T = 10^3\,\mathrm{K}$ and a λ^{-2} emissivity, only slightly hotter than the curve in Fig. 6*a*. Both approaches therefore indicate that the color temperature of the non-stellar NIR continuum is close to $10^3\,\mathrm{K}$. The fractional energy contained in the NIR spectral region is about 10% in Fig. 6*a* and about 17% in Fig. 6*b*.

Next we consider whether the NIR excess continuum is correlated with AFE emission. In Fig. 7, we plot the ratio of the average $4\,\mu$m emission (taken to be representative of the NIR excess emission) to the mean flux density of AFE(7.7), against $\log L_{\mathrm{FIR}}/L_{\mathrm{B}}$. (The two methods of removing the stellar continuum, discussed above, lead to more or less the same $4\,\mu$m fluxes.) The strength of AFE($7.7\,\mu$m) relative to the J-band flux increases by nearly an order of magnitude within the sample (see Table 2), as $L_{\mathrm{FIR}}/L_{\mathrm{B}}$ increases. On the other hand, there is no net trend in Fig. 7, indicating that the NIR excess correlates strongly with the MIR emission for galaxies with a wide range in dust content and luminosity. We view this as strong evidence that the NIR excess continuum originates in the ISM, as opposed to being (scattered) starlight from late-type stars or circumstellar dust emission. However, the scatter in Fig. 7 is greater than can be accounted for by measurement errors, suggesting that there are some real variations among galaxies in the ratio of the NIR excess to AFE(7.7). The most deviant point is the early-type galaxy NGC 5866, which, as mentioned in §3.2.5, has very weak AFE features.

This non-stellar dust continuum is probably the same component that has been detected in reflection nebulae and the large-scale ISM of our own Galaxy (see §1). In fact, Sellgren

et al. (1985) showed that, for the reflection nebulae NGC 7023 and NGC 2023, the 4 μm emission surface brightness is between 1/6 to 1/10 of that at the peak of AFE(7.7). This range is quantitatively consistent with our results in Fig. 6. It has been suggested that such a NIR continuum might be due to electronic fluorescence or a quasi-continuum of overlapping bands of PAH molecules (e.g., Allamandola, Tielens, & Barker 1989). While further work is needed in order to determine whether the AFEs and NIR continuum emission arise from exactly the same macromolecules or material, it seems clear that the carriers of these two components are closely related.

In Table 5 we summarize the luminosity in the NIR region relative to the FIR dust emission, for each of the three subsamples defined in §2.1. The total NIR luminosity is $5-18\%\,L_{\rm FIR}$ and arises mostly from stellar photospheres. If we correct for the stellar contribution using the two methods described above, the non-stellar NIR continuum contributes $\sim 3-4\%\,L_{\rm FIR}$ for the most quiescent galaxies in our sample, and $1-2\%\,L_{\rm FIR}$ for the most FIR-active ones. These estimates are on the same order as the *COBE* results for our own Galaxy (Bernard et al. 1994).

4.2. Variations in the Mid-Infrared AFEs

Some variations have been observed among Galactic sources in the profiles of the AFEs (e.g., Roelfsema et al. 1996; Peeters et al. 2002) and the ratios of one feature relative to another (e.g., Joblin et al. 1996; Lu 1998; Vermeij et al. 2002), but the physical implications are still not fully understood. In particular, it appears that relative strengths of the features are quite insensitive to the intensity and color temperature of the local radiation field (e.g., Uchida et al. 2000; Chan et al. 2001). Likewise, while we find similar variations in the AFEs in our sample of galaxies, we have not found any statistically significant correlation between these variations and $L_{\rm FIR}/L_{\rm B}$, $R(60/100)$, optical morphology, the 7 μm-to-15 μm flux density ratio (Dale et al. 2000), or the mean surface brightness at 7 or 15 μm within an isophotal ellipse containing 50% of the infrared flux.

In Fig. 8 we plot the ratios of the strengths of the 6.2, 8.6, and 11.3 μm AFEs to AFE(7.7) against $L_{\rm FIR}/L_{\rm B}$ for the 40 galaxies, which all show clearly discerned AFEs. We hereafter abbreviate the mean F_λ of a feature by its wavelength, e.g. (6.2) for the mean flux of AFE(6.2). There is some indication of a slight decreasing trend in these plots. However, these trends are weak and probably not statistically significant. We computed the median feature strength ratios separately for the FIR-quiescent, intermediate, and FIR-active subsamples defined in §2.1. The values are given in Table 6 and plotted as large crosses in Fig. 8. It can be seen that the median values decline by less than 1 σ_s from FIR-quiescent to FIR-

active, where σ_s is the r.m.s. dispersion of the entire sample (see the last row of Table 6). This differs from the conclusion of Lu et al. (1999) that the ratio (11.3)/(7.7) decreases with increasing $L_{\rm FIR}/L_{\rm B}$. That earlier study was based on an older PHT-S calibration, but more importantly, the stellar continuum was removed in a more simplistic way, by subtracting a power-law fit to the spectral intervals 3.5–5 μm and 9.5–10.5 μm. That procedure had the effect of undersubtracting the continuum underlying the 11.3 μm feature in galaxies with a strong stellar component, thus producing an apparent trend.

The scatter in Fig. 8 is significantly greater than the statistical error bars, implying that there are intrinsic galaxy-to-galaxy variations in the relative feature strengths. According to Table 6, the spread in the AFE ratios is $\sim 15\%$ for (6.2)/(7.7) and (8.6)/(7.7), and $\sim 25\%$ for (11.3)/(7.7). Within the framework of the PAH hypothesis, variations in the relative feature strengths have been attributed to the presence of different fractions of PAHs that are ionized and/or hydrogenated, as a consequence of differences in the ambient UV radiation field (e.g., Jourdain de Muizon et al. 1990; de Frees et al. 1993; Schutte et al. 1993; Langhoff 1996). However, our data suggest that the situation may be more complex than a simple dependence on the UV radiation field. It is plausible that chemical processing may also play an important role in determining the local abundance and emission properties of the PAHs (e.g., Boulanger et al. 1990).

The spectra in Fig. 2 also show some galaxy-to-galaxy variations in the AFE profiles. In Appendix C, we quantify one aspect of these variations by defining a "logarithmic slope" S that measures the steepness of the feature profile on the short- or long-wavelength side. As we show in Table C1, the galaxy-to-galaxy variations in S range from 15–30% for all the AFEs, except for the short-wavelength side of AFE(8.6) which shows possibly much greater variations relative to the median value. This could either be due to intrinsic variations in the profile of AFE(8.6), or to a contribution from a weak feature around 8.2 μm that varies from galaxy to galaxy. Such a shorter-wavelength feature was invoked by Verstraete et al. (2001) to fit high-S/N ISO-SWS spectra of Galactic sources, and an emission feature at $\sim 8.2\,\mu$m has also been observed in some post-AGB stars (Peeters et al. 2002).

4.3. The Destruction of the AFE Carriers

It was previously known that the AFEs are depressed in H II regions (e.g., Césarsky et al. 1996). This has been widely attributed to the preferential destruction of the small AFE carriers relative to larger dust grains in these regions. *IRAS* data also indicate an AFE depression over galaxy scales, with the AFEs being more severely depressed in galaxies with warmer $R(60/100)$ colors (Helou, Ryter, & Soifer 1991).

Fig. 9 shows how L_{AFEs}, the summed luminosity of the four MIR AFEs (6.2, 7.7, 8.6, and 11.3 μm), correlates with $L_{\rm FIR}$. The few galaxies without a PHT-S aperture coverage factor p in Table 2 are not plotted here. We indicate galaxies with values of $p < 35\%$ (for which the aperture correction is large and therefore less certain) by filled symbols, in order to distinguish them from the others (open symbols). For some of these galaxies, Malhotra et al. (2001, Table C1) have derived G_0, the intensity of the far-UV interstellar radiation field in units of the radiation field in the solar neighborhood, based on a PDR model that depends on the observed fluxes in [C II] 158 μm and [O I] 63 μmand the flux of the total infrared emission. These galaxies are plotted as squares of three different sizes, where the smallest corresponds to $2.3 \leq \log G_0 < 3.4$, the intermediate size to $3.5 \leq \log G_0 < 3.9$, and the largest to $4.0 \leq \log G_0 < 4.8$.

For comparison, we also show in Fig. 9 the *IRAS* results of Werner, Gautier, & Cawlfield (1994) for multiple spatial positions in two Galactic H II regions, the Rosette and California nebulae (indicated by a dashed line), and the reflection nebula in the Pleiades (indicated by a solid line). These lines actually represent the logarithmic ratio of the *IRAS* 12 μm flux (assumed to be proportional to our integrated AFE flux) to the FIR flux, and are shifted vertically in order to bracket most of the galaxy data points. The average trend of our galaxy points is steeper than that characteristic of the reflection nebula, but shallower than the trend for the H II regions. This comparison suggests that both H II regions and reflection nebulae contribute to the total AFE and FIR emission of galaxies.

In Table 7 we list median ratios of several different measures of the AFE overall intensity to the FIR flux, for the three subsamples. It can be seen from the table that the depression of AFEs relative to the FIR emission becomes significant only for the most FIR-active subsample; for the latter galaxies, $L_{\rm AFEs}/L_{\rm FIR}$ has a value only 60% that of the other two subsamples. Furthermore, from Fig. 9 it can be seen that this AFE depression is more related to the hardness than the intensity of the radiation field: at a given $R(60/100)$, galaxies with higher values of G_0 tend to lie closer to the dashed line. Since the flux ratio of [C II] to the AFEs has very little dispersion in this sample of galaxies (Helou et al. 2001), one does expect such a linkage between the diagnostics based on the fine-structure lines and the AFEs. However, this is unlikely just a mathematical linkage, for the two reference lines in Fig. 9 clearly suggest that the (UV-hard) HII regions have a lower $L_{\rm AFEs}/L_{\rm FIR}$ than the (UV-soft) reflection nebulae at any given $R(60/100)$.

If the photodestruction process that weakens the AFEs in Galactic H II regions is also responsible for depressing the AFE emission on galaxy scales, our results imply that the mass spectrum of the dust particles could differ significantly between quiescent and starburst galaxies.

As shown in §3.1, the MIR emission from disk galaxies is dominated by strong AFE emission over a wide range in such physical characteristics as the intensity of the interstellar UV radiation field, FIR luminosity, and temperature of the FIR-emitting dust. The few exceptions we find may be indicative of the extreme conditions required for the AFEs to fade from view. Representing the high-radiation-field limit, we have objects such as NGC 4418 (which may be an AGN), IC 860, and NGC 1569 (which, if plotted in Fig. 9 despite its small value for p, would lie near the position of IC 860). For these objects, it is reasonable to explain the weakness of the AFEs as being the consequence of destruction of the AFE carriers by hard UV photons (or shocks), by analogy with the Galactic sources discussed above.

It is less clear what causes the deficiency in AFE emission in the FIR-quiescent galaxy NGC 5866. This is the earliest type galaxy in Key Project sample for which we have a PHT-S spectrum; unfortunately, we did not obtain PHT-S observations for the other three E/S0 galaxies in our program (Malhotra et al. 2000). The lack of strong AFE emission in NGC 5866 could be due either to an actual deficiency of the AFE carriers or to a lack of energetic UV photons capable of exciting the features, or both. Note that our LWS observations of the [C II] 158 μm and [O I] 63 μm lines indicate a particularly weak and soft UV radiation field in this galaxy (Malhotra et al. 2000).

5. Summary

We present new *ISO* PHT-S spectra (2.5–11.6 μm), extended to 1.25 μm using *JHK* data from the 2MASS survey, for a sample of 45 disk galaxies that span the typical range in global properties of galaxies energetically dominated by star formation. PHT-S aperture coverage factors are also provided for most of the galaxies. We decompose the spectra into three constituents: (1) stellar continuum emission, which dominates at the shortest wavelengths (2.5–4.9 μm; NIR); (2) a weaker and redder NIR "excess continuum"; and (3) the well-known aromatic dust emission features (AFEs) at 6.2, 7.7, 8.6, and 11.3 μm which dominate the long-wavelength half of the PHT-S spectra (5.8–11.6; MIR). Most of the galaxy spectra appear similar to each other, especially in the MIR region, and to an averaged "template" spectrum shown in Fig. 3. The most striking exceptions are NGC 4418, which shows no AFEs but instead has a broad mid-infrared continuum upon which is superposed a strong 10 μm silicate absorption feature; and NGC 1569, which has a very weak infrared continuum but an unusually strong [S IV] 10.5 μm line from ionized gas.

The non-stellar NIR excess continuum has an average color temperature of $\sim 10^3$ K and a luminosity of a few percent of $L_{\rm FIR}$, where $L_{\rm FIR}$ is the far-infrared (40–120 μm) luminosity

attributed to large dust grains. This NIR continuum scales more or less linearly with the strength of the AFEs, suggesting that the NIR excess continuum originates in the ISM of galaxies (and not, for example, in late-type stars or circumstellar dust); and that the AFEs and NIR excess continuum arise from similar carriers.

The profiles and relative strengths of the AFEs in the disk galaxies match those of "Type A" mid-infrared spectra, by far the most predominant type of mid-infrared dust emission pattern in the ISM of our own Galaxy. This resemblance suggests that the carriers of the Type-A AFEs are also prevalent in the ISM of other galaxies. The combined luminosity of the AFEs in the region 5.8–11.3 μm is 10–20% $L_{\rm FIR}$. The relative strengths of the AFEs vary on average by 15–25%. These observed variations, however, do not correlate with *IRAS* 60 μm-to-100 μm flux density ratio, $R(60/100)$, or the far-infrared-to-blue luminosity ratio $L_{\rm FIR}/L_{\rm B}$, two commonly used indicators of global star-formation activity in galaxies. We interpret this as indicating that other factors, in addition to the present-day radiation field, affect the strengths and shapes of the AFEs.

The ratios of both the AFEs and non-stellar NIR continuum to the FIR flux decrease systematically from the most quiescent galaxies to the most actively star-forming galaxies in the sample. We show that this is more related to the hardness than the intensity of the heating radiation field, likely a result of the AFE/NIR carriers being preferentially destroyed, relative to the larger dust grains responsible for the FIR emission, in regions of active star formation and intense UV radiation fields. This implies that the mass and size distribution functions of the interstellar dust particles vary in environments with different levels of star formation activity.

We are grateful to J. A. Acosta-Pulido for his help on the PHT-S flux calibrations, and to the other Key Project members, J. Brauher, A. Contursi, D. Hollenbach, D. A. Hunter, M. Kaufman, S. Kolhatkar, K.-Y. Lo, S. D. Lord, R. H. Rubin, G. J. Stacey, and H. A. Thronson, Jr., for their contributions to the project from which this paper was derived. We thank the anonymous referee for a number of comments that improved the presentation of this paper. The *ISO* Photometer, ISO-PHOT, was built by Lemke et al. (1996). The data presented here were reduced with the ISOPHOT Interactive Analysis (PIA) package, a joint development by the ESA Astrophysics Division and the ISOPHOT Consortium with the collaboration of the Infrared Processing and Analysis Center (IPAC). This work was supported in part by *ISO* data analysis funding from the National Aeronautics and Space Administration (NASA), and has made use of the NASA/IPAC Extragalactic Database (NED) which is maintained by the Jet Propulsion Laboratory, California Institute of Technology, under contract with NASA.

A. Flux Comparison of the PHT-S and ISO-CAM Data

ISO-CAM LW2 images are available for 42 galaxies in Table 1 from Dale et al. (2000), and for one additional galaxy, NGC 5866, in the ISO archive from the observations described by Vigroux et al. (1999). For each of these galaxies, we integrated the LW2 filter curve over the PHT-S spectrum to derive $f_p(LW2)$, a CAM LW2-equivalent flux density at 6.7 μm. The LW2 bandpass extends to about 5 μm on the short-wavelength side. For its wavelength coverage beyond the blue end of the SL array, we used a simple linear interpolation between the red end of the SS array and the blue end of the SL.

We then centered the PHT-S aperture on the CAM image at the position of our PHT-S observation. Because a CAM filter-wheel jitter can affect the effective pointing of CAM images, a small residual positional uncertainty remains. After subtracting a constant sky level from the CAM image, we derived the quantity $f_c(LW2)$ by integrating the source surface brightness over the PHT-S aperture. As a result, we have

$$f_c(LW2) = \int_{24'' \times 24''} SB(x,y) dx dy, \qquad (A1)$$

where $SB(x,y)$ is the source surface brightness distribution function. We can express $f_p(LW2)$ in a similar way:

$$f_p(LW2) = (1/f_{psf}) \int B(x,y)\, SB(x,y) dx dy, \qquad (A2)$$

where f_{psf} is the fractional point-source spread function for PHT-S and $B(x,y)$ is the PHT-S beam profile (which has a value of unity near the aperture center). We have implicitly assumed that f_{psf}, $B(x,y)$, and $SB(x,y)$ are all effective values over the PHT-S detector pixels included within the CAM LW2 bandpass. The integration in eq. (A1) is over the PHT-S aperture only, while that in eq. (A2) is over the entire source. For a source that is sufficiently compact that it can be treated as a point source with respect to the PHT-S beam profile, one has $f_c(LW2)/f_p(LW2) \approx f_{psf}$. For the PHT-S detector pixels relevant to the CAM LW2 filter, $f_{psf} \approx 0.92$. Therefore, for point sources we should have $f_c(LW2)/f_p(LW2) \approx 0.92$, if there were no systematic flux offset between the two instruments.

Fig. 10 is a plot of $f_c(LW2)/f_p(LW2)$ as a function of p, the fractional CAM LW2 flux of a galaxy that falls within the PHT-S aperture, which is given by the ratio of $f_c(LW2)$ to the total LW2 flux of the galaxy. Notice that the scatter is larger for more extended sources (i.e., smaller values of p); this effect may be partly due to the residual positional uncertainty described above. In addition, $f_c(LW2)/f_p(LW2)$ increases on average as p drops, presumably due to the beam size effect in eq. (A1). The average flux ratio for the 20 galaxies with $p > 0.6$ is (0.76 $\pm$0.03) and is indicated by the dotted line in Fig. 10. This implies

a possible systematic flux difference of no greater than 18% between the CAM LW2 and PHT-S results.

A similar comparison was performed with the CAM LW1 (4–5 μm) data (Dale et al. 2000) on the 10 galaxies for which these data were available. The result is shown in Fig. 11. The scatter in this diagram is significantly greater than in Fig. 10, largely because the galaxies are much fainter in LW1. Nevertheless, a quantitatively similar result is found as for the LW2 comparison: the median flux ratio in Fig. 11 is 0.7, which implies a difference of about 25% in flux scale after taking f_{psf} into account.

B. Zero-Point Difference between the PHT-S and 2MASS Fluxes

Using the 2MASS K-band flux density and the average PHT-S 4 μm flux density as defined in Table 2, we show here that the zero-point offset between the 2MASS and PHT-S flux scales is insignificant. In Fig. 12*a* we plot $f_\nu(4\,\mu\mathrm{m})$ against $f_\nu(K)$ for our sample galaxies. The dotted line is a least-squares fit to all the data points, by minimizing their distances perpendicular to the fit, and intercepts the vertical axis at about (0.006 ± 0.005) Jy. However, we believe that this overestimates the true zero-point offset. In fact, $f_\nu(4\,\mu\mathrm{m})/f_\nu(K)$ should rise somewhat as $\log L_{\rm FIR}/L_{\rm B}$ increases, because the contribution of the non-stellar 3–5 μm continuum emission (see §4.1) has a greater influence on $f_\nu(4\,\mu\mathrm{m})$ than on $f_\nu(K)$. Indeed, Fig. 12*b* shows that there are more FIR-active galaxies at smaller K fluxes. A better estimate of the zero-point offset in flux is therefore given by the solid line in Fig. 12*a*, which is a similar least-squares fit but includes only those galaxies with $\log L_{\rm FIR}/L_{\rm B} < 0.1$ (which are shown as solid squares in both Figs. 12*a* and 12*b*). This line has a vertical interception of only (0.002 ± 0.007) Jy. We therefore conclude that the zero-point offset between the PHT-S and SMASS flux scale is insignificant.

C. Slopes of Feature Profiles

For each AFE, we define a "logarithmic slope" parameter S that measures the steepness of the feature profile on the short or long- wavelength side,

$$S = \frac{I_0 - I_1}{I_0 + I_1}, \qquad (C1)$$

where I_0 is the flux density of the detector pixel nearest the peak of the emission feature in the rest-frame, and I_1 is the flux density of a detector pixel down one side of the feature. For I_0 we used the pixel corresponding to 6.216 μm in Table 3 for AFE(6.2), 7.616 μm for

AFE(7.7), 8.540 μm for AFE(8.6) and 11.263 μm for AFE(11.3). For simplicity we chose I_1 at one of the detector pixels that was used to define the wavelength range of the feature (see Table 2). Two slopes can be defined for each AFE, S_- for the short-wavelength side and S_+ for the long-wavelength side, except for AFE(11.3), for which only $S_-(11.3)$ can be defined.

In Table C1, we list for each AFE: the median value for the 40-galaxy sample defined in §3.1 [Col. (2)]; the r.m.s. dispersion around this median [Col. (3)]; and σ_m, the median of the statistical measurement errors [Col. (4)]. While the ratio of Cols. (3) to (2) tells us about the variation in the slope, the ratio of Cols. (3) to (4) can be used to gauge whether this is significant. The ratio of Cols. (3) to (2) ranges from $\sim$ 15–30% for both slopes of AFE(6.2) and AFE(7.7) and for $S_+(8.6)$, to 40% for $S_-(11.3)$, to 130% for $S_-(8.6)$. The ratios of Cols. (3) to (4) show that, of these, only the variations in $S_-(8.6)$ are significant at $3\,\sigma_m$. Possible reasons for the observed variations in $S_-(8.6)$ are discussed §4.2.

REFERENCES

Ables, H. D. 1971, Publ. U.S. Naval Obs. 20, Part IV, 60

Allamandola, L. J, Tielens, A. G. G. M., & Barker, J. R. 1985, ApJ, 290, L25

———. 1989, ApJS, 71, 733

Andriesse, C. D. 1978, A&A, 66, 169

Arp, H., & Sandage, A. 1985, AJ, 90, 1163

Athey, A., Bregman, J., Bregman, J., Temi, P., & Sauvage, M. 2002, ApJ, 571, 272

Bakes, E. L., & Tielens, A. G. G. M. 1994, ApJ, 427, 822

Beintema, D.A., et al. 1996, A&A, 315, L369

Bernard, J. P., Boulanger, F., Désert, F. X., Giard, M., Helou, G., & Puget, J. L. 1994, A&A, 291, L5

Boulanger, F., Boisssel, P., Césarsky, D., Ryter, C. 1998, A&A, 339, 194

Boulanger, F. et al. 1996, A&A, 315, L325

Boulanger, F., Falgarone, E., Puget, J.-L., & Helou, G. 1990, ApJ, 364, 136

Bregman, J. D. 1989, in Interstellar Dust, IAU Symposium 135, ed. L. J. Allamandola and A. G. G. M. Tielens, (Dordrecht: Kluwer), 109

Bregman, J. D., Dinerstein, H. L., Goebel, J. H., Lester, D. F., Witteborn, F. C., & Rank, D. M. 1983, ApJ, 274, 666

Bridle, A. H., & Perley, R. A. 1984, ARA&A, 22, 319

Bruzual, G., & Charlot, S. 1993, ApJ, 405, 538

Bushouse, H. A., Telesco, C. M., & Werner, M. W. 1998, AJ, 115, 938

Césarsky, D., Lequeux, J., Abergel, A., Perault, M., Palazzi, E., Madden, S., & Tran, D. 1996, A&A, 315, L309

Chan, K.-W., Roellig, T. L., Onaka, T., Mizutani, M., Okumura, K., Yamamura, I., Tanabé, T., Shibai, H., Nakagawa, T., & Okuda, H. 2001, ApJ, 546, 273

Clavel, J, et al. 2000, A&A, 357, 839

Cohen, M., Allamandola, L. J., Tielens, A. G. G. M., Bregman, J. D., Simpson, J. P., Witteborn, F. C., Wooden, D. H., Rank, D. M. 1986, ApJ, 302, 737

Cohen, M., & Volk, K. 1989, AJ, 98, 1563

Condon, J. J., Helou, G., Sanders, D. B., & Soifer, B. T. 1990, ApJS, 73, 359

Dale, D. A. et al. 2000, AJ, 120, 583

Dale, D. A., Helou, G., Contursi, A., Silbermann, N. A., & Kolhatkar, S. 2001, ApJ, 549, 215

de Frees, D. J., Miller, M. D., Talbi, D., Pauzat, F., & Ellinger, Y. 1993, ApJ, 408, 530

de Vaucouleurs, G. & Capaccioli, M. 1979, ApJS, 40, 699

de Vaucouleurs, G., de Vaucouleurs, A., Corwin, H. G., Buta, R. J., Paturel, G., & Fouqué, P. 1991, Third Reference Catalogue of Bright Galaxies (New York: Springer)

Duley, W. W., & Williams, D. A. 1981, MNRAS, 196, 269

———. 1988, MNRAS, 230, 1

Frogel, J. A., Persson, S. E., Aaronson, M., & Matthews, K. 1978, ApJ, 220, 75

Gabriel et al. 1997, in Astronomical Data Analysis Software and Systems VI, ed. G. Hunt & H. E. Payne (San Francisco: ASP), Vol. 125, 108

Geballe, T.R. 1997, in From Stardust to Planetesimals, ASP Conference 122, ed. Y.J. Pendleton & A.G.G.M. Tielens (San Francisco: ASP), 119

Genzel, R., et al. 1998, ApJ, 498, 579

Gillett, F.C., Forrest, W.J. & Merrill, K. 1973, ApJ, 183, 87

Greggio, L., Tosi, M., Clampin, M., de Marchi, G., Leitherer, C., Nota, A., Sirianni, M. 1998, ApJ, 504, 725

Helou, G. 1986, ApJ, 311, 33

Helou, G. et al. 1997, BAAS, 191, 240

Helou, G., Lu, N. , Werner, M. W., Malhotra, S., & Silbermann, N. 2000, ApJ, 532, L21 (Paper I)

Helou, G., Malhotra, S., Hollenbach, D.J., Dale, D.A., & Contursi, A. 2001, ApJ, 548, L73

Helou, G., Ryter, C., & Soifer, B. T. 1991, ApJ, 376, 505

Hibbard, J. E., & van Gorkom, J. H. 1996, AJ, 111, 655

Hudgins, D.M., Allamandola, L.J., & Sandford, S.A. 1997, Adv. Space Res., 19, 999

Hunter, D. A., et al. 2001, ApJ, 553, 121

Israel, F. P. 1988, A&A, 194, 241

Israel, F. P., & van Driel, W. 1990, A&A, 236, 323

Jarrett, T. H. 2000, PASP, 112, 1008

Jarrett, T. H. Chester, T., Cutri, R., Schneider, S., & Huchra, J. 2003, AJ(in press)

Joblin, C., Tielens, A. G. G. M., Geballe, T. R., & Wooden, D. H. 1996, ApJ, 460, 119

Jourdain de Muizon, M., d'Hendecourt, L. B., & Geballe, T. R. 1990, A&A, 227, 526

Kessler, M.F., et al. 1996, A&A, 315, L27

Knapp, G. R., Gunn, J. E., & Wynn-Williams, C. G. 1992, ApJ, 399, 76

Langhoff, S. R. 1996, J. Phys. Chem. 100, 2819

Leech, K. J., Penston, M. V., Terlevich, R., Lawrence, A., Rowan-Robinson, M., & Crawford, J. 1989, MNRAS, 240, 349

Léger, A., & Puget, J. L. 1984, A&A, 137, L5

Lemke, D. et al. 1996, A&A, 315, L64

Lemke, D., Mattila, K., Lehtinen, K., Laureijs, R. J., Liljestrom, T., Leger, A., & Herbstmeier, U. 1998, A&A, 331, 742

Lu, N. 1998, ApJ, 498, L65

Lu, N., et al. 1999, ESASP, 427, 929

Lu, N., & Hur, M. 2000, BAAS, 196, 2702

———. 2003, (in preparation)

Luhman, M.L., et al. 1998, ApJ, 504, L11

Malhotra, S., et al. 1997, ApJ, 491, L37

———. 2000, ApJ, 543, 634

———. 2001, ApJ, 561, 766

Mathis, J. S. 1990, ARA&A, 28, 37

Mattila, K., Lemke, D., Haikala, L. K., Laureijs, R. J., Leger, A., Lehtinen, K., Leinert, C., Mezger, P. G. 1996, A&A, 315, L353

Peeters, E., Hony, S., Van Kerckhoven, C., Tielens, A. G. G. M., Allamandola, L. J., Hudgins, D. M., & Bauschlicher, C. W. 2002, A&A, 390, 1089

Persson, S. E., Frogel, J. A., & Aaronson, M. 1979, ApJS, 39, 61

Puget, J. L., & Léger, A. 1989, A&A, 27, 161

Rank, D. M., Dinerstein, H. L., Lester, D. F., Bregman, J. K., Aitken, D. K., & Jones, B. 1978, MNRAS, 185, 179

Reach, W. T., Boulanger, F., Contursi, A., and Lequeux, J. 2000, A&A, 361, 895

Rigopoulou, D., Spoon, H. W. W., Genzel, R., Lutz, D., Moorwood, A. F. M., & Tran, Q. D. 1999, AJ, 118, 2625

Roche, P.F., Aitken, D.K., Smith, C. H. & James, S. D. 1986, MNRAS, 218, 19P

Roche, P.F., Aitken, D.K., Smith, C. H. & Ward, J. 1991, MNRAS, 248, 606

Roelfsema, P. R., et al. 1996, A&A, 315, L289

Schutte, W., Tielens, A. G. G. M., & Allamandola, L. J. 1993, ApJ, 415, 397

Sellgren, K. 1984, ApJ, 277, 623

Sellgren, K., Allamandola, L. J., Bregman, J. D., Werner, M. W., & Wooden, D. H. 1985, ApJ, 299, 416

Sellgren, K., Werner, M. W., & Dinerstein, H. L. 1983, ApJ, 271, L13

Soifer, B. T., Boehmer, L., Neugebauer, G., & Sanders, D. B. 1989, AJ, 98, 766

Spoon, H. W. W., Keane, J. V., Tielens, A. G. G. M., Lutz, D., & Moorwood, A. F. M. 2001, A&A, 365, L353

Stanford, S. A., & Balcells, M. 1990, ApJ, 355, 59

———. 1991, ApJ, 370, 118

Sturm, E., Lutz, D., Tran, D., Feuchtgruber, H., Genzel, R., Kunze, D., Moorwood, A. F. M., & Thornley, M D. 2000, A&A, 358, 481

Tanaka, M., Matsumoto, T., Murakami, H., Kawada, M., Noda, M., & Matsuura, S. 1996, PASJ, 48, L53

Thuan, T. X., Sauvage, M., & Madden, S. 1999, ApJ, 516, 783

Tokunaga, A.T. 1997, in Diffuse Infrared Radiation and the IRTS, ASP Conf. Ser., Vol. 124, ed. H. Okuda, Matsumoto, T., & Roellig, T. (San Francisco: ASP), 149

Uchida, K. I., Sellgren, K., Werner, M. 1998, ApJ, 493, 109

Uchida, K. I., Sellgren, K., Werner, M. W., & Houdashelt, M. L. 2000, ApJ, 530, 817

Vermeij, R., Peeters, E., Tielens, A.G.G.M., & van der Hulst, J.M. 2002, A&A, 382, 1042

Verstraete, L., et al. 2001, A&A, 372, 981

Verstraete, L., Puget, J. L., Falgarone, E., Drapatz, S., Wright, C. M., & Timmermann, R. 1996, A&A, 315, L337

Vigroux, L., et al. 1999, in Universe as Seen by ISO, ed. P. Cox & M. F. Kessler (ESA SP-427; Noordwijk: ESA), 805

Waller, W. H. 1991, ApJ, 370, 144

Werner, M. W., Gautier, T. N., & Cawlfield, T. 1994, in The First Symposium on the Infrared Cirrus and Diffuse Interstellar Clouds, ed. R. M. Cutri & W. B. Latter (ASP Conf. Ser), Vol 58, 270

Wilson, W. J., Schwartz, P. R., Neugebauer, G. 1972, ApJ, 177, 523

AAS LaTeX macros v5.0.

Table 1. Galaxy Properties

Galaxy (1)	R.A.[a] (2)	Dec[a] (3)	ROLL[b] (4)	ISO-TDT[c] (5)	Morphology[d] (6)	log L_B^e (7)	log $L_{\rm FIR}/L_{\rm B}{}^f$ (8)
NGC 278	05204.6	473301	73.03	59702263	SAB(rs)b	9.77	0.01
NGC 520	12435.0	34742	247.28	77702280	Irr	10.33	0.36
NGC 693	15030.9	60841	67.88	59502319	I0:sp	9.61	0.13
NGC 695	15114.2	223456	66.50	63300751	IB?(s)m:pec	10.85	0.50
NGC 1022	23832.5	-64038	244.41	78401024	(R')SB(s)a	9.83	0.26
UGC 02238	24617.4	130544	72.90	63301036	Pec	10.21	0.82
NGC 1222	30856.8	-25717	258.14	82400843	S0- pec:	9.87	0.44
NGC 1317	32244.7	-370609	201.48	75001077	SAB(r)a	10.03	-0.40
NGC 1326	32356.4	-362749	201.39	75001158	(R)SB(rl)0/a	9.84	-0.28
NGC 1385	33728.2	-243004	241.72	79600846	SB(s)cd	10.06	-0.03
UGC 02855	34822.9	700759	94.09	62902698	SB(s)cd II-III	10.12	0.31
NGC 1482	35439.4	-203007	240.50	79600986	SA0+ pec sp	9.54	0.93
NGC 1546	41436.6	-560338	124.41	68900662	SA?a pec	9.72	-0.22
NGC 1569 C	43049.1	645052	90.07	64600492	IBm	9.33	-0.66
———— NW	43046.6	645057	244.83	64600492	.....	....	....
———— SE	43051.7	645045	244.87	64600492	.....	....	....
NGC 2388	72853.5	334905	94.06	71802365	SA(s)b: pec	9.80	1.11
ESO 317-G023	102442.4	-391822	328.02	25200171	(R')SB(rs)a	9.90	0.53
NGC 3583	111410.7	481901	292.74	19500259	SB(s)b	10.27	-0.18
NGC 3620	111604.8	-761252	340.02	27600983	(R')SB(s)ab	....	....
NGC 3683	112732.1	565242	294.46	19401040	SB(s)c?	9.75	0.42
NGC 3705	113006.8	91638	295.43	18400677	SAB(r)ab	9.68	-0.62
NGC 3885	114646.6	-275523	307.94	25200727	SA(s)0/a	9.86	0.04
NGC 3949	115341.5	475131	299.79	19500332	SA(s)bc:	9.65	-0.19
NGC 4027	115930.6	-191547	299.65	24200368	SB(s)dm	10.01	-0.08
NGC 4102	120623.3	524240	301.90	19500586	SAB(s)b?	9.52	0.54
NGC 4194	121410.0	543142	303.81	19401376	IBm pec	9.97	0.63
NGC 4418	122654.7	-05242	292.74	24100408	(R')SAB(s)a	9.47	1.15

Table 1—Continued

Galaxy (1)	R.A.[a] (2)	Dec[a] (3)	ROLL[b] (4)	ISO-TDT[c] (5)	Morphology[d] (6)	log L_B^e (7)	log $L_{\rm FIR}/L_{\rm B}{}^f$ (8)	R
NGC 4490	123036.8	413823	299.88	20501580	SB(s)d pec	9.91	-0.21	
NGC 4519	123330.5	83916	290.87	23600331	SB(rs)d	9.46	-0.30	
NGC 4691	124813.4	-31958	292.86	23101069	(R)SB(s)0/a pec	9.62	-0.02	
IC 3908	125640.5	-73342	293.15	25202254	SB(s)d?	9.33	0.29	
IC 860	131503.5	243707	281.96	61800104	SB(s)a:	9.66	1.05	
IC 883	132035.3	340824	301.38	21501377	Pec	10.23	1.14	
NGC 5433	140236.0	323037	314.85	57100315	SAB(s)c:	10.25	0.33	
NGC 5713	144011.3	-01724	281.31	28400959	SAB(rs)bc pec	10.15	0.20	
NGC 5786	145856.9	-420045	298.09	29900767	(R')SAB(s)bc	10.69	-0.49	
NGC 5866	150629.4	554546	273.89	26902854	S0	9.79	-0.60	
NGC 5962	153631.7	163632	279.95	27800783	SA(r)c	10.20	-0.09	
IC 4595	162044.2	-700835	268.25	27601375	SB?c sp II:	10.28	0.14	
NGC 6286	165831.8	585612	355.19	20700516	SB(s)0+ pec?	10.16	0.83	
NGC 6753	191123.7	-570256	247.95	29901232	(R)SA(r)b	10.55	-0.02	
NGC 7218	221011.7	-163936	249.17	36902415	SB(r)c	9.88	-0.17	
NGC 7418	225635.9	-370145	243.31	36902723	SAB(rs)cd	9.97	-0.32	
IC 5325	232843.1	-411957	237.82	36902824	SAB(rs)bc	9.88	-0.26	
NGC 7771	235124.9	200641	66.54	21900879	SB(s)a	10.69	0.41	
Mrk 331	235126.2	203508	73.52	56500644	SA(s)a: pec	10.09	1.12	

[a]J2000 Right Ascension and Declination in "hhmmss.s" and "ddmmss," respectively.

[b]The ISO roll angle in degrees, measured in a counterclockwise manner from the celestial north to the which is perpendicular to the direction in which the chopper was operated for sky reference positions. T the sky orientation of the square aperture of PHT-S which is aligned with the spacecraft axes.

[c]The TDT number of the ISO observation as it appears in the ISO archive.

[d]Optical morphology taken from Dale et al. (2000) if available, otherwise from the RC3 catalog (de Vauco

[e]Logarithmic optical blue luminosity in solar units, derived as in Dale et al. (2000).

[f]Logarithmic FIR-to-blue luminosity ratio, derived as in Dale et al. (2000).

[g]*IRAS* 60 μm-to-100 μm flux density ratio, derived from *IRAS* addscan fluxes [see Table 4 of Dale et al.

[h]Heliocentric velocity in units of km s^{-1}.

Table 2. Mean Flux Densities F_λ around Selected Wavelengths[a]

Galaxy (1)	p[b] (2)	J[c] (3)	H[c] (4)	K[c] (5)	4μm[d] (6)	(6.2)[e] (7)	(7.7)[e] (8)	(8.6)[e] (9)	(11.3) (10)
NGC 278	0.31	27.46	18.48	8.27	0.87(0.13)	1.93(0.03)	2.79(0.02)	1.39(0.02)	1.46(0.
NGC 520	0.23	9.77	8.05	4.40	0.57(0.13)	1.33(0.03)	1.82(0.03)	0.51(0.03)	0.21(0.
NGC 693	0.72	12.63	9.45	4.70	0.92(0.09)	1.02(0.03)	1.27(0.02)	0.73(0.03)	0.66(0.
NGC 695	0.73	7.75	5.40	2.75	0.92(0.12)	1.83(0.03)	2.72(0.02)	1.30(0.03)	.... (...
NGC 1022	0.78	13.09	10.23	4.95	0.65(0.08)	2.18(0.03)	3.37(0.02)	1.68(0.02)	1.42(0.
UGC 02238	0.80	5.07	4.26	2.45	0.66(0.11)	1.91(0.03)	2.91(0.02)	1.37(0.04)	1.15(0.
NGC 1222	0.76	8.56	6.22	2.85	0.84(0.10)	1.65(0.03)	2.29(0.02)	1.14(0.02)	1.14(0.
NGC 1317	....	37.42	25.44	11.40	1.42(0.09)	0.62(0.02)	0.73(0.02)	0.46(0.02)	0.48(0.
NGC 1326	0.70	50.08	34.37	15.54	1.30(0.26)	1.23(0.02)	1.59(0.01)	0.89(0.02)	0.94(0.
NGC 1385	0.29	13.14	8.86	3.93	0.45(0.07)	1.13(0.02)	1.69(0.02)	0.89(0.02)	0.80(0.
UGC 02855	0.08	16.19	13.80	7.02	0.80(0.13)	1.04(0.03)	1.72(0.03)	0.81(0.03)	0.80(0.
NGC 1482	0.66	22.08	19.36	10.48	2.47(0.07)	5.88(0.03)	9.33(0.03)	4.05(0.02)	3.79(0.
NGC 1546	0.33	21.24	15.66	7.21	0.84(0.18)	1.53(0.05)	2.09(0.04)	1.09(0.03)	1.29(0.
NGC 1569 C	0.22	25.33	16.51	7.47	1.05(0.09)	0.46(0.02)	0.35(0.02)	0.24(0.03)	0.30(0.
———— NW	0.32	18.02	11.75	5.43	0.98(0.10)	0.82(0.03)	0.79(0.03)	0.66(0.02)	0.96(0.
———— SE	0.15	12.61	8.28	3.72	0.38(0.09)	0.35(0.03)	0.38(0.02)	0.24(0.02)	0.26(0.
NGC 2388	0.84	11.19	8.75	4.40	0.69(0.11)	1.75(0.04)	2.59(0.06)	1.24(0.03)	0.87(0.
ESO 317-G023	0.74	10.48	8.07	4.08	0.76(0.10)	1.11(0.03)	1.88(0.02)	0.89(0.03)	0.92(0.
NGC 3583	0.37	19.57	13.82	6.40	1.20(0.11)	0.87(0.03)	1.17(0.02)	0.60(0.02)	0.69(0.
NGC 3620	0.75	30.99	27.11	14.64	2.33(0.11)	3.95(0.04)	6.38(0.03)	2.89(0.02)	1.78(0.
NGC 3683	0.47	18.21	14.35	7.07	1.25(0.11)	2.09(0.04)	2.90(0.02)	1.33(0.02)	0.91(0.
NGC 3705	0.20	20.28	14.60	6.57	0.85(0.09)	0.50(0.05)	0.39(0.03)	0.20(0.02)	0.07(0.
NGC 3885	0.82	26.73	19.72	9.51	1.83(0.14)	1.87(0.03)	2.57(0.03)	1.30(0.03)	1.40(0.
NGC 3949	0.24	14.47	10.04	4.35	0.47(0.10)	0.77(0.04)	1.06(0.02)	0.51(0.02)	0.55(0.
NGC 4027	....	7.83	5.32	2.30	0.37(0.08)	0.69(0.03)	0.89(0.03)	0.39(0.02)	0.31(0.
NGC 4102	0.62	45.15	34.18	17.04	3.39(0.14)	4.44(0.03)	6.78(0.03)	3.36(0.03)	2.94(0.
NGC 4194	0.81	11.84	8.62	4.27	0.42(0.13)	2.47(0.03)	3.68(0.03)	1.68(0.02)	1.02(0.
NGC 4418	0.84	6.68	4.57	2.09	0.47(0.11)	1.35(0.04)	2.86(0.03)	1.23(0.02)	0.29(0.

Table 2—Continued

Galaxy (1)	p^b (2)	J^c (3)	H^c (4)	K^c (5)	4μm^d (6)	(6.2)^e (7)	(7.7)^e (8)	(8.6)^e (9)	(11.3)^e (10)
NGC 4490	0.05	13.87	8.66	3.62	0.58(0.12)	0.40(0.03)	0.41(0.03)	0.22(0.02)	0.33(0.03)
NGC 4519	0.27	4.62	3.17	1.31	0.39(0.11)	0.36(0.03)	0.46(0.03)	0.25(0.03)	0.11(0.04)
NGC 4691	....	13.09	8.70	3.94	0.91(0.16)	1.94(0.07)	2.69(0.04)	1.39(0.04)	1.38(0.06)
IC 3908	0.52	11.51	8.80	4.42	0.84(0.11)	1.51(0.03)	2.14(0.01)	0.77(0.12)	0.95(0.05)
IC 860	0.89	5.30	3.76	1.73	0.28(0.03)	0.20(0.01)	0.31(0.01)	0.12(0.01)	0.16(0.02)
IC 883	0.90	3.88	2.83	1.53	0.56(0.12)	1.26(0.03)	1.90(0.03)	0.76(0.02)	0.43(0.04)
NGC 5433	0.71	7.62	5.90	2.99	0.72(0.12)	1.23(0.05)	1.90(0.02)	0.87(0.04)	0.74(0.07)
NGC 5713	0.45	16.58	11.34	5.26	1.66(0.13)	2.30(0.04)	3.34(0.03)	1.64(0.04)	1.73(0.07)
NGC 5786	0.30	11.42	8.37	3.80	0.83(0.11)	0.66(0.03)	0.84(0.02)	0.46(0.03)	0.39(0.05)
NGC 5866	0.61	64.78	46.92	22.32	3.32(0.11)	0.87(0.04)	0.68(0.02)	0.38(0.02)	0.41(0.04)
NGC 5962	0.30	22.20	14.70	6.71	0.53(0.13)	0.72(0.04)	1.05(0.02)	0.61(0.02)	0.40(0.07)
IC 4595	0.34	9.90	8.58	4.32	0.75(0.11)	1.04(0.04)	1.45(0.02)	0.68(0.02)	0.70(0.05)
NGC 6286	0.69	7.71	6.41	3.55	0.90(0.14)	1.56(0.06)	2.44(0.02)	1.00(0.02)	0.87(0.06)
NGC 6753	0.33	38.53	28.44	13.21	1.64(0.10)	1.19(0.02)	1.40(0.02)	0.70(0.02)	0.82(0.03)
NGC 7218	0.36	8.23	5.58	2.45	0.41(0.10)	0.58(0.03)	0.78(0.02)	0.35(0.02)	0.35(0.04)
NGC 7418	0.12	5.45	3.70	1.69	-0.11(0.14)	0.30(0.03)	0.32(0.02)	0.13(0.02)	0.09(0.04)
IC 5325	0.22	9.98	6.84	3.02	0.23(0.08)	0.48(0.02)	0.59(0.02)	0.24(0.02)	0.23(0.05)
NGC 7771	0.52	17.35	13.41	6.70	1.16(0.10)	1.80(0.04)	2.74(0.03)	1.34(0.03)	1.13(0.07)
Mrk 331	0.76	8.98	6.72	3.46	0.80(0.12)	1.82(0.04)	2.73(0.02)	1.32(0.03)	1.22(0.07)
NGC 3379	....	119.31	79.66	34.94	4.81(0.06)	0.86(0.02)	0.50(0.01)	0.48(0.01)	0.39(0.03)
NGC 4374	....	99.70	71.52	31.67	3.77(0.06)	0.61(0.01)	0.41(0.01)	0.40(0.01)	0.36(0.02)

[a]All flux densities are in units of $10^{-14}\,\mathrm{W\,m^{-2}\,\mu m^{-1}}$. To convert between this unit and Jy, we use 1.25, 1.65, 2.2, 4 μm as the effective wavelengths for Columns (3), (4), (5) and (6), respectively. The parenthesized value following a flux density is the statistical error of that flux.

[b]PHT-S aperture coverage factor p as defined in Appendix A.

[c]JHK flux densities within the PHT-S aperture.

[d]The mean 4 μm flux density derived from a simple average of the flux densities in Jy of the 27 pixel channels between 3.4 and 4.4 μm.

[e]The mean flux density of an AFE, defined as the integrated flux between λ_1 and λ_2 divided by $(\lambda_2 - \lambda_1)$, where λ_1 and λ_2 are respectively 5.98 μm and 6.64 μm for AFE(6.2), 7.20 μm and 8.22 μmfor AFE(7.7), 8.22 μm and 9.23 μmfor AFE(8.6), and 10.86 μm and 11.40 μmfor AFE(11.3).

Table 3. Rest-Frame Average Spectra[a]

$\lambda(\mu\mathrm{m})$ (1)	Norm. at J[b] (2)	Norm. by (7.7)[c] (3)	n[d] (4)	Ellipticals[e] (5)
1.250	1.000(0.000)	1.000(0.166)	40	1.000(0.000)
1.650	1.283(0.017)	1.364(0.201)	40	1.200(0.043)
2.200	1.093(0.026)	1.223(0.164)	40	0.940(0.038)
2.469	0.707(0.030)	0.794(0.111)	40	0.551(0.076)
2.510	0.683(0.037)	0.796(0.107)	40	0.493(0.050)
2.550	0.758(0.037)	0.843(0.123)	40	0.511(0.040)
2.591	0.773(0.033)	0.903(0.115)	40	0.547(0.002)
2.631	0.811(0.029)	0.889(0.128)	40	0.518(0.041)
2.671	0.823(0.037)	0.914(0.132)	40	0.532(0.032)
2.712	0.776(0.038)	0.926(0.114)	40	0.492(0.035)

[a]The complete vesrion of this table is in the electronic edition of the Journal. The printed edition contains only a sample. The average spectra are shown in f_ν, all normalized to have 1 Jy at J. The standard deviation of the mean is given in the parentheses following each flux.

[b]Individual spectra normalized at J.

[c]Individual spectra normalized by AFE(7.7).

[d]Number of galaxies used in the averaging.

[e]The average spectrum of the 2 ellipticals using the J-band normalization scheme. Note that the AFE(7.7) normalization scheme would lead to essentially the same average spectrum for the ellipticals.

Table 4. Infrared Lines and Emission Features

Wavelength (μms)	Identifications	EW (μm)
3.30	AFE(3.3)	0.02
4.03	Brα?	0.06
6.2	AFE(6.2)	....
7.0	[Ar II] 6.99μm + AFE(6.9) + H_2 0-0 S(5)	0.003
7.7	AFE(7.6/7.7)	....
8.6	AFE(8.6)	....
10.6	[S IV] 10.51μm	0.002
11.3	AFE(11.3)	....

Table 5. Median NIR-to-FIR Flux Ratios

Subsample (1)	No.[a] (2)	$R(60/100)^b$ (3)	$\log L_{\rm FIR}/L_{\rm B}{}^b$ (4)	$\rm NIR^{total}/FIR^b$ (5)	$\rm NIR^{ISM}_{rc}/FIR^b$ (6)	$\rm NIR^{ISM}_{zr}/FIR^b$ (7)
FIR-quiescent	12	0.39 (0.06)	-0.18 (0.24)	0.174 (0.10)	0.028 (0.03)	0.041 (0.03)
Intermediate	11	0.52 (0.08)	0.37 (0.35)	0.083 (0.06)	0.019 (0.02)	0.035 (0.02)
FIR-active	13	0.73 (0.09)	0.54 (0.39)	0.043 (0.04)	0.013 (0.03)	0.020 (0.03)

[a]Actual number of galaxies in each subsample.

[b]Median ratios, each followed in the parentheses by the r.m.s. dispersion with respect to the median. Columns (5) to (7) are the ratios of the integrated PHT-S flux over 2.5 to 4.7 μm to the FIR flux by treating the stellar continuum differently: no stellar continuum is removed in Column (5), and it is removed in both Columns (6) and (7) using the reddening corrected and zero-reddening methods, respectively.

Table 6. Median Flux-Density Ratios of the AFEs

No.[a] (1)	$\log L_{FIR}/L_B^b$ (2)	$(6.2)/(7.7)^b$ (3)	$(8.6)/(7.7)^b$ (4)	$(11.3)/(7.7)^b$ (5)
13	-0.21(0.16)	0.69(0.12)	0.48(0.07)	0.46(0.13)
13	0.20(0.15)	0.69(0.05)	0.48(0.08)	0.47(0.11)
13	0.82(0.27)	0.65(0.04)	0.46(0.04)	0.40(0.09)
All	0.20(0.46)	0.66(0.09)	0.47(0.06)	0.45(0.12)

[a]Number of galaxies in each subsample. The last row is for the whole sample.

[b]Median ratios, each followed in parentheses by the r.m.s. dispersion with respect to that median.

Table 7. Median MIR-to-FIR Flux Ratios

Subsample[a] (1)	(5.8-11.3)/FIR[b] (2)	AFEs(6-9)/FIR[b] (3)	AFEs/FIR[b] (4)
FIR-quiescent	0.18 (0.06)	0.13 (0.05)	0.15 (0.05)
Intermediate	0.17 (0.04)	0.13 (0.04)	0.15 (0.04)
FIR-active	0.11 (0.05)	0.09 (0.04)	0.09 (0.04)

[a]Same subsamples as in Table 5.

[b]Column (2) is the median ratio of the integrated flux between 5.8 and 11.3 μm to the FIR flux. Column (3) is the median ratio of the summed flux of AFE(6.2), AFE(7.7) and AFE(8.6) to the FIR flux. Column (4) is the median ratio of the summed flux of all the 4 MIR features to the FIR flux. Each median flux ratio is followed in the parentheses by the r.m.s. dispersion with respect to that median. PHT-S aperture correction has been applied to all the MIR fluxes.

Table C1. Feature Profile Slopes

Profile Slope[a] (1)	Median (2)	Dispersion[b] (3)	σ_m^c (4)
$S_-(6.2)$	0.69	0.14	0.05
$S_+(6.2)$	0.42	0.14	0.06
$S_-(7.7)$	0.49	0.08	0.03
$S_+(7.7)$	0.33	0.08	0.03
$S_-(8.6)$	0.09	0.12	0.04
$S_+(8.6)$	0.55	0.15	0.10
$S_-(11.3)$	0.58	0.24	0.11

[a]S_- and S_+ refer to the profile slopes at the short- and long-wavelength sides of an emission feature, respectively.

[b]The r.m.s dispersion with respect to the median.

[c]Median of the statistical measurement errors in the profile slope.

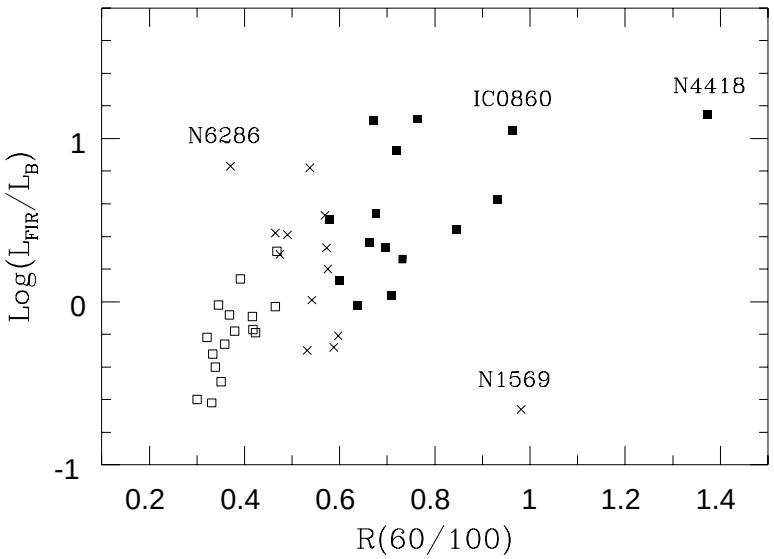

Fig. 1.— Distribution of the galaxies in a plot of $\log L_{\rm FIR}/L_{\rm B}$ *vs.* $R(60/100)$. The sample is divided into an "FIR-quiescent" subsample (open squares), an "FIR-active" subsample (solid squares), and an intermediate subsample (crosses). NGC 3620, for which L_B is not available, was assigned to the intermediate subsample, and is omitted from Figs. 1, 7, and 8.

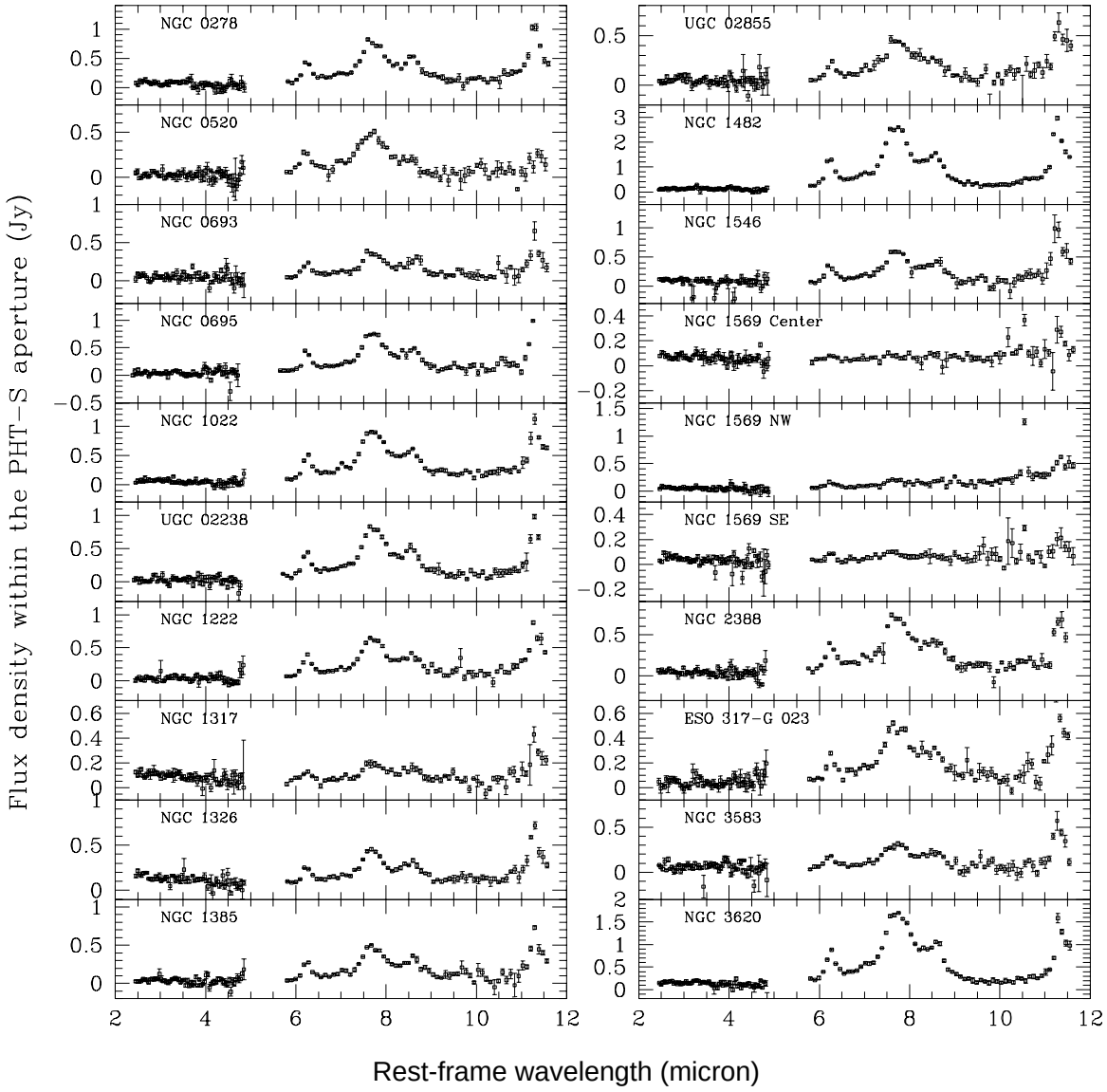

Fig. 2.— PHT-S spectra in units of Jy as a function of the rest-frame wavelength in microns. The error bars show the statistical errors for each spectral point.

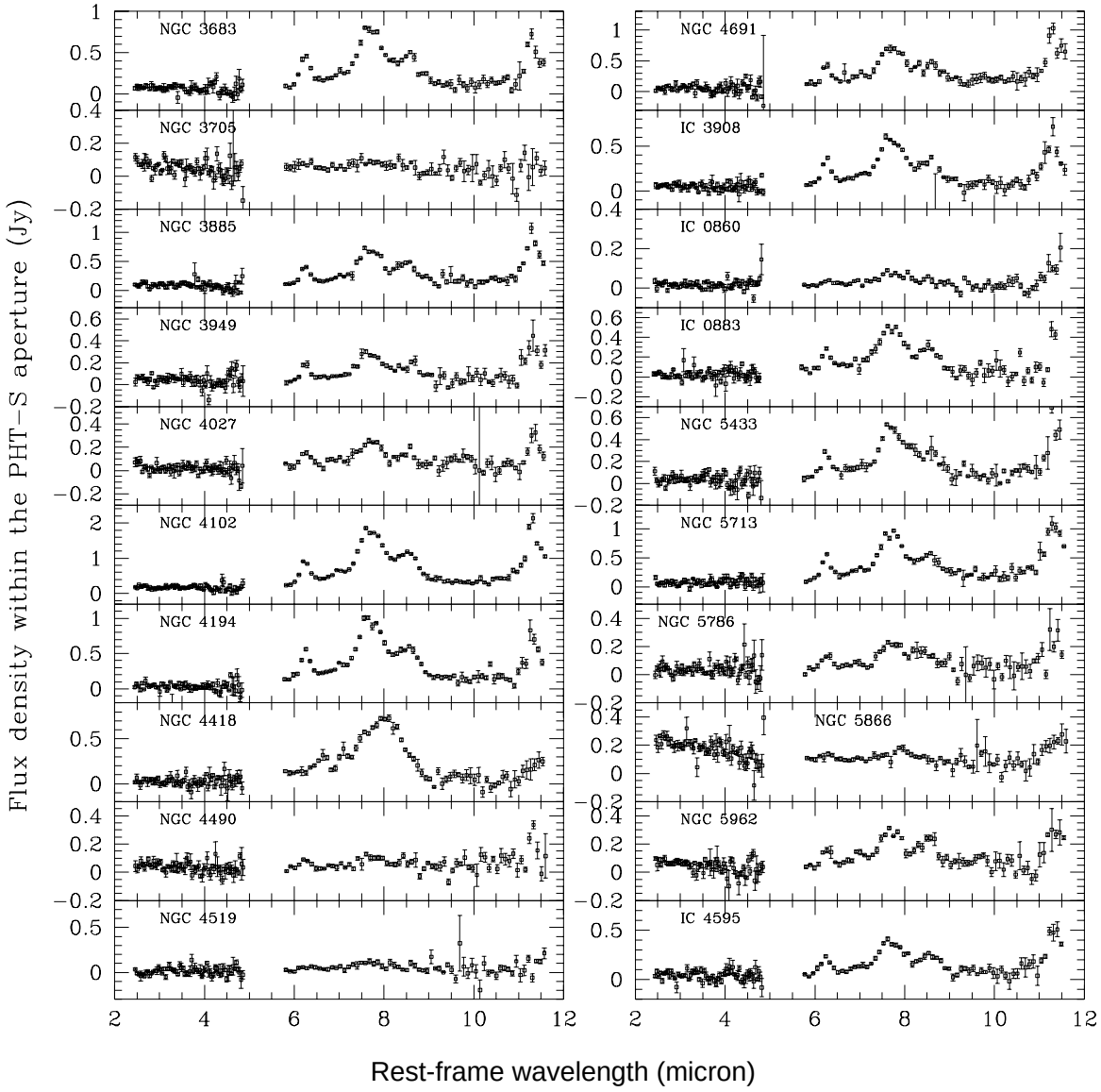

Fig. 2.— Continuation of Fig. 2*a*.

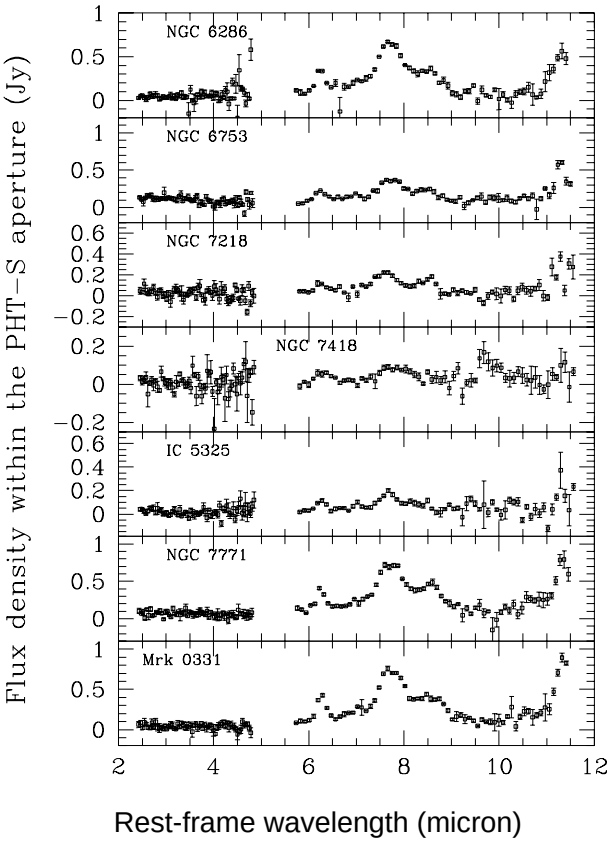

Fig. 2.— Continuation of Fig. 2*a*.

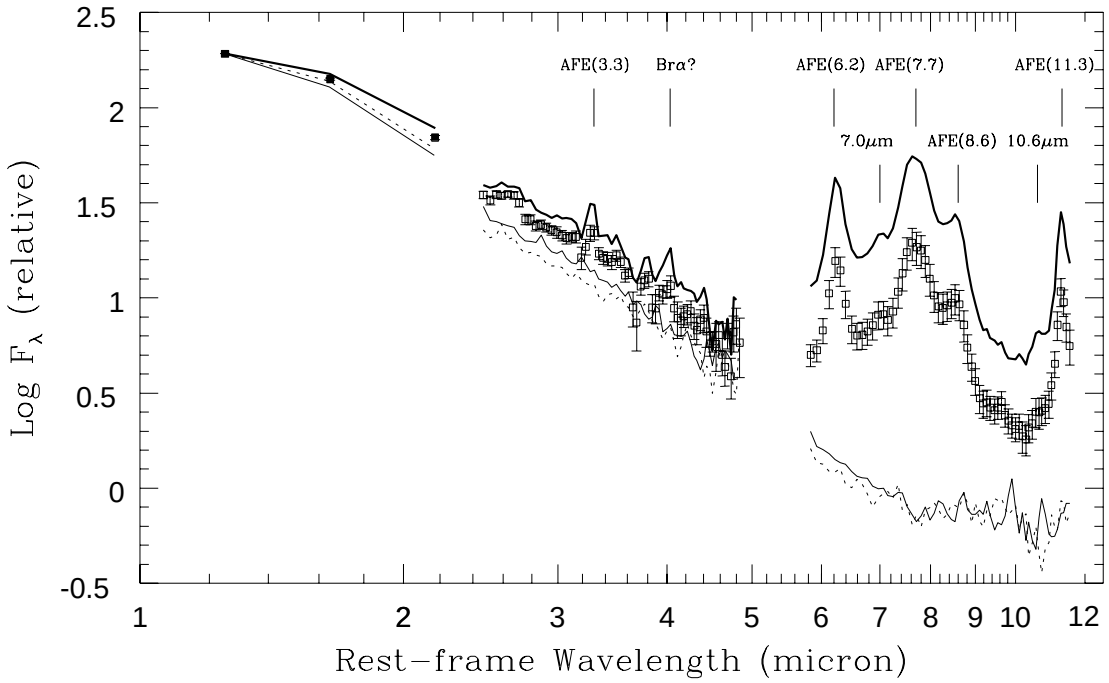

Fig. 3.— Plots of the average rest-frame spectra derived from weighted averages of the spectra of 40 galaxies (see §3.1). The squares represent the average spectrum obtained by normalizing to the J fluxes, while the thick solid curve results from normalizing by the integrated flux of AFE(7.7 μm). Representative error bars are shown only for the former; note that the error bars should smallest near the fiducial wavelength used for the normalization. The spectra of two elliptical galaxies are also shown: NGC 3379 (the thin solid curve) and NGC 4374 (the dotted line).

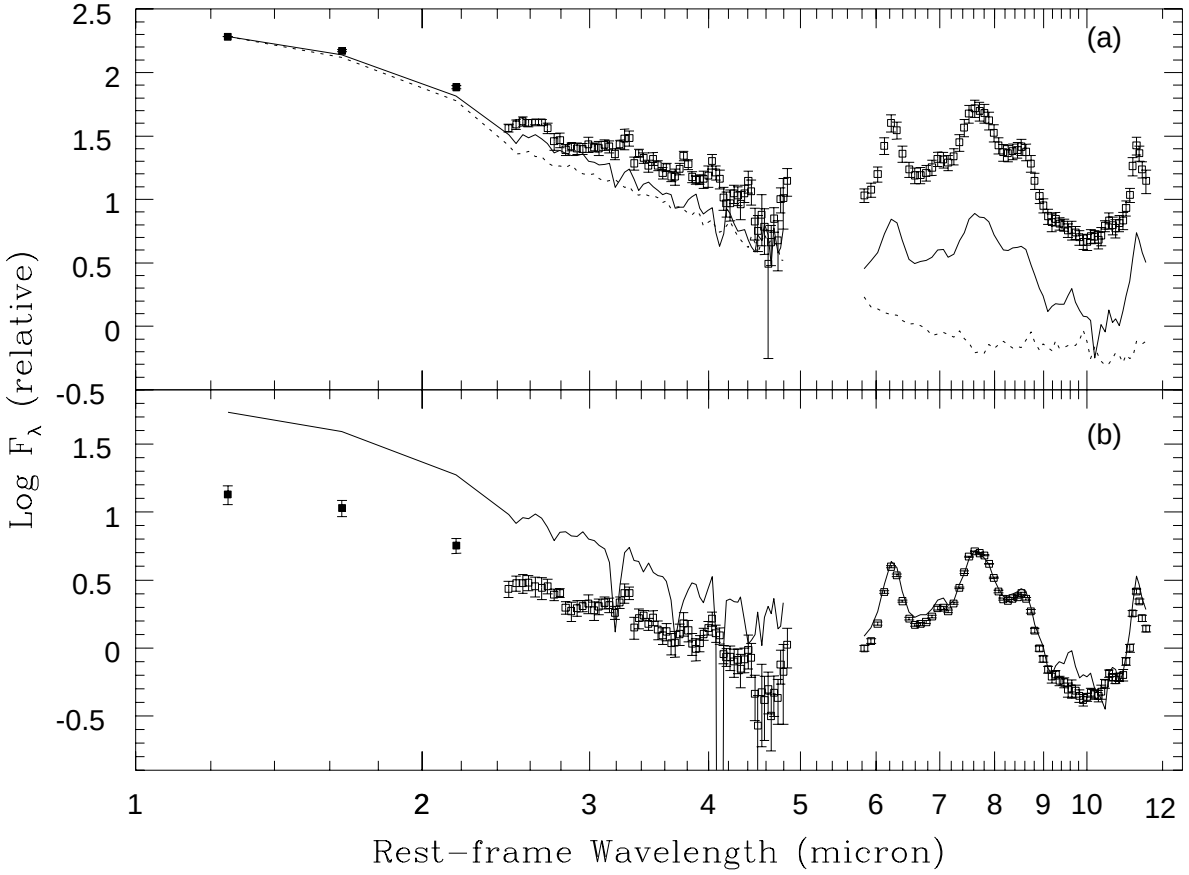

Fig. 4.— Comparison of the average spectra of the FIR-quiescent and FIR-active subsamples (see §2.1; also Table 5). The squares represent the FIR-active subsample and the solid curve is the average spectrum of the FIR-quiescent galaxies. The mean of the elliptical galaxy spectra is shown as a dotted curve. (Numerical values for all three curves can be found in Table 3.) As explained in the text, different normalizations are used for generating the spectra in (a) and (b).

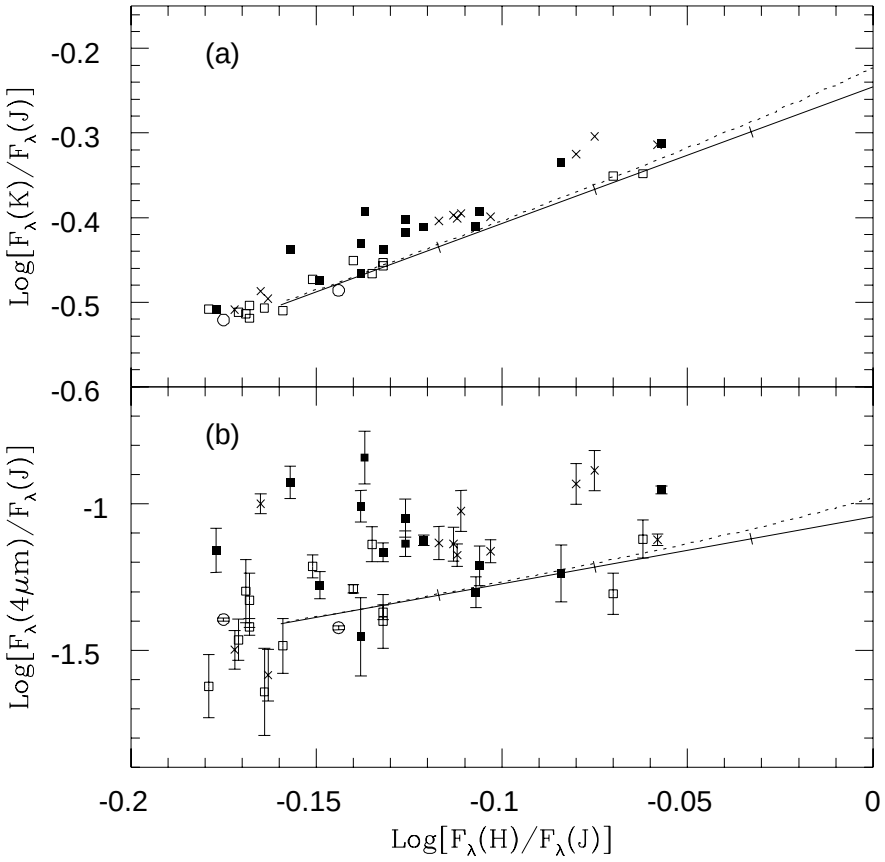

Fig. 5.— Near-IR "color-color" plots: (*a*) log $F_\lambda(K)/F_\lambda(J)$ *vs.* log $F_\lambda(H)/F_\lambda(J)$, and (*b*) log $F_\lambda(4\mu\mathrm{m})/F_\lambda(J)$ *vs.* log $F_\lambda(H)/F_\lambda(J)$, where $F_\lambda(4\mu\mathrm{m})$ is the mean flux density at 4μm as defined in Table 2. The Key Project galaxies are shown as open squares, solid squares, and crosses (as in Fig. 1), and the reference elliptical galaxies as circles. In each panel, the solid line is the inferred reddening line for the case of a foreground dust screen the dotted curve is for the case where dust and stars are uniformly mixed. The tick marks along the solid line indicate respectively $\mathrm{A}_V = 1$, 2, and 3^m for the dust screen case.

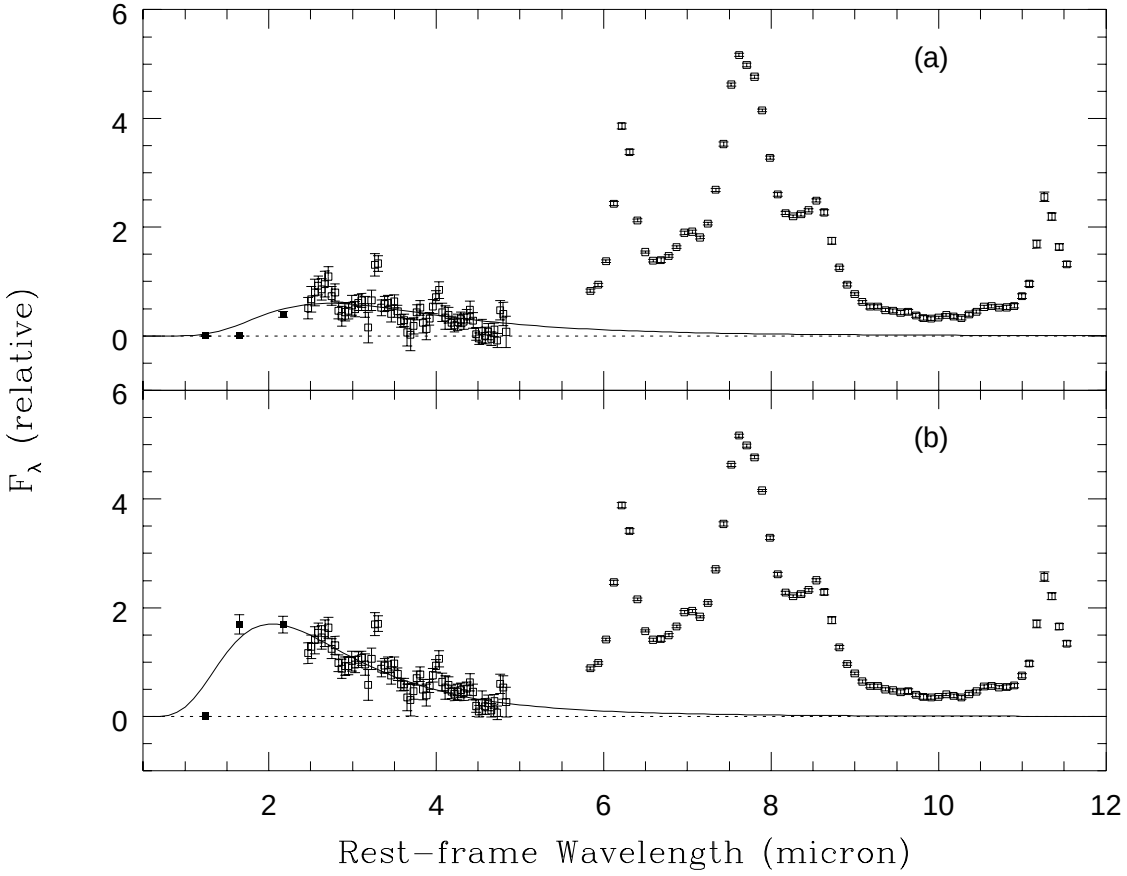

Fig. 6.— Averaged spectra obtaining by subtracting from each disk galaxy spectrum (a) a stellar continuum reddened to agree with the H/J color, or (b) an unreddened stellar continuum (derived from the elliptical galaxies.) The solid curves are modified black-bodies with an emissivity that scales as λ^{-2} and $T = 750\,\mathrm{K}$ in (a) and $10^3\,\mathrm{K}$ in (b). The error bars represent the standard deviation of the mean. The individual, stellar continuum-subtracted spectra were normalized by the integrated flux of AFE(7.7) prior to averaging, and the results are renormalized to the same peak flux of the $7.7\,\mu$m feature.

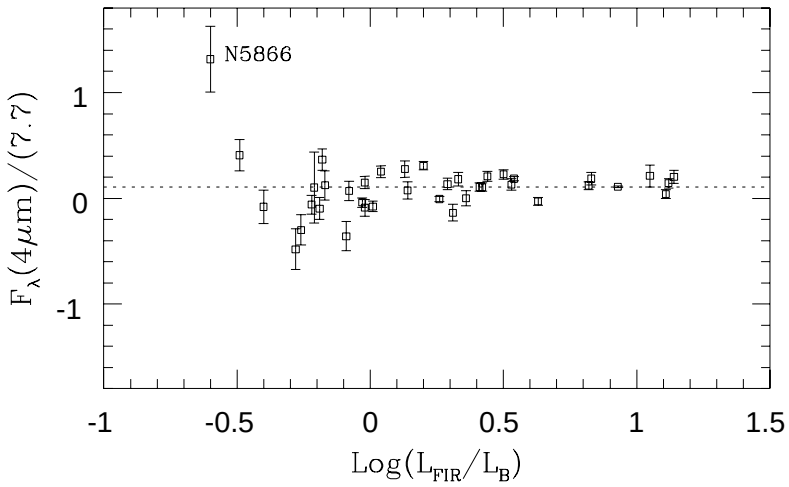

Fig. 7.— Plot of the ratio of the flux density at 4μm to the mean flux density AFE(7.7), as a function of $L_{\rm FIR}/L_{\rm B}$. Both $F_\lambda(4\,\mu{\rm m})$ and (7.7) were computed after removal of the stellar contributions. The dotted line indicates the median sample flux ratio of 0.11.

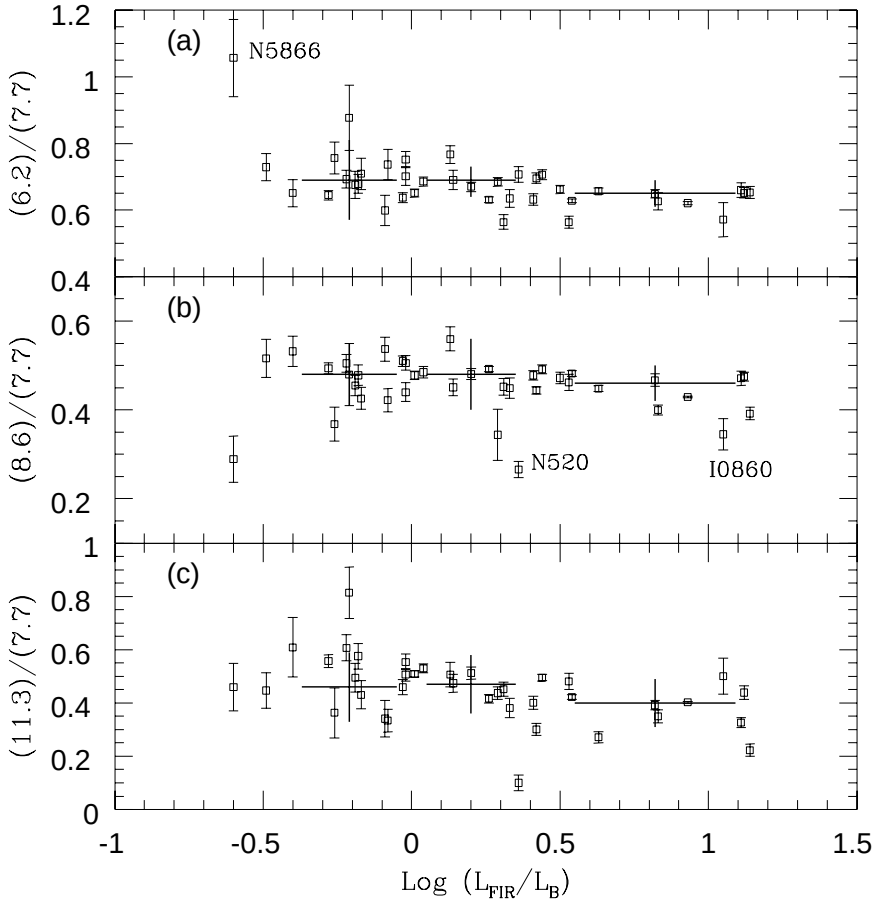

Fig. 8.— Plots of the relative strengths of the AFEs as a function of $L_{\rm FIR}/L_{\rm B}$, where (6.2)/(7.7), (8.6)/(7.7), (11.3)/(7.7) represent the mean F_λ for these features after removal of the stellar continuum (using the zero-reddening method). We have divided the data set into three equal-size subsamples in terms of $L_{\rm FIR}/L_{\rm B}$, and plotted their median values as large crosses in each plot. The extent of each cross indicate the r.m.s. dispersion with respect to the median value for each subsample. A few outliers are labelled.

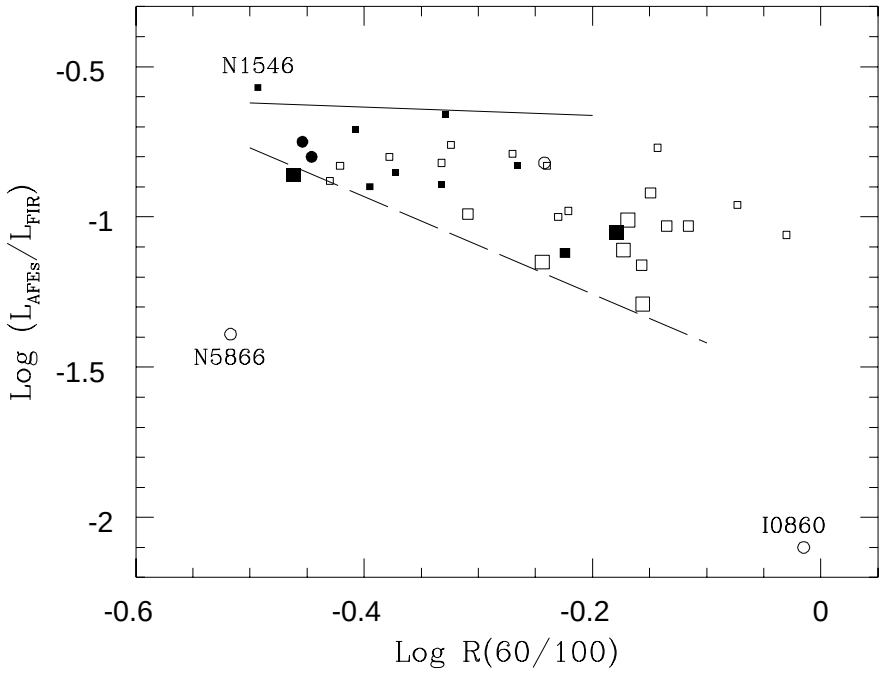

Fig. 9.— Plot of the ratio of the combined luminosity of the AFEs to the FIR dust emission, as a function of $R(60/100)$. Galaxies with (without) a measured interstellar far-UV radiation field G_0 in Malhotra et al. (2001) are represented by squares (circles). The sizes of the squares represent the approximate value of G_0, and the filled symbols represent galaxies with the largest aperture corrections, as described in the text. The statistical errors in $L_{\rm AFEs}/L_{\rm FIR}$ are small and thus no error bars are plotted. Note that nearly all of the galaxies fall within a wedge defined by the solid and dotted lines, derived from *IRAS* observations of reflection nebulosity and H II regions respectively.

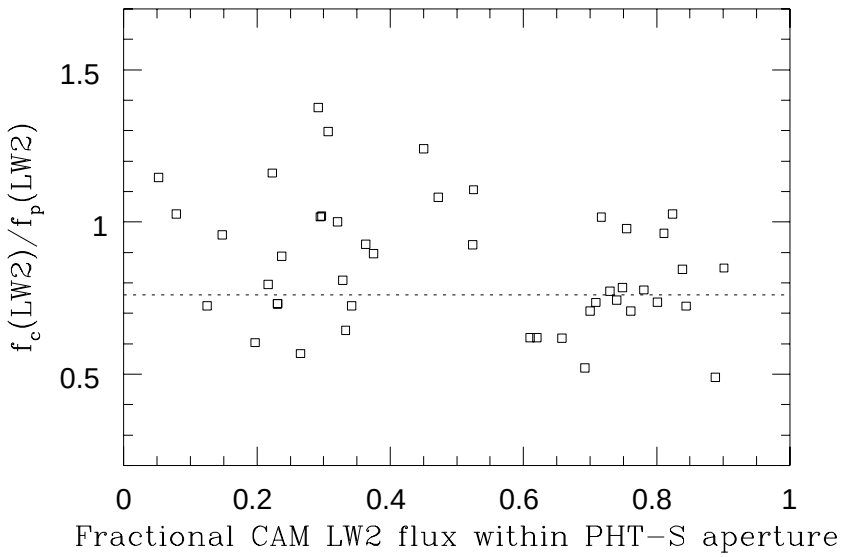

Fig. 10.— Comparison of the PHT-S flux scale with the flux scale of CAM in the LW2 filter ($\lambda_0 = 6.7\,\mu$m). The abscissa is p, the fraction of the galaxy flux at $6.7\,\mu$m that falls within the PHT-S $24'' \times 24''$ aperture. The ordinate is the ratio of the CAM LW2 flux within the PHT-S aperture to a CAM LW2-band-equivalent flux derived from the PHT-S spectrum. The dotted line indicates a ratio of 0.76, the mean value for the 20 sources with $p > 0.6$.

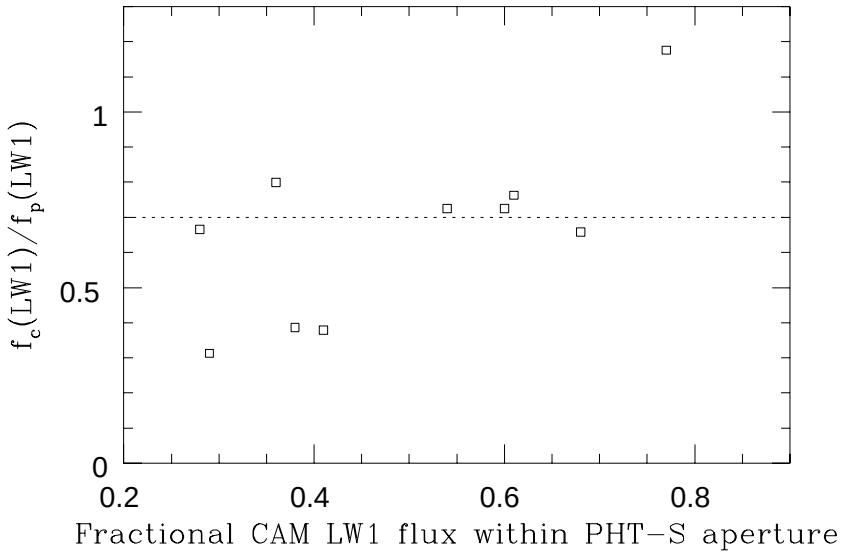

Fig. 11.— Similar to Fig. 10, but comparing with CAM LW1 (4 to 5 μm) data. The dotted line indicates a flux ratio of 0.7, the median value of the data shown in the plot.

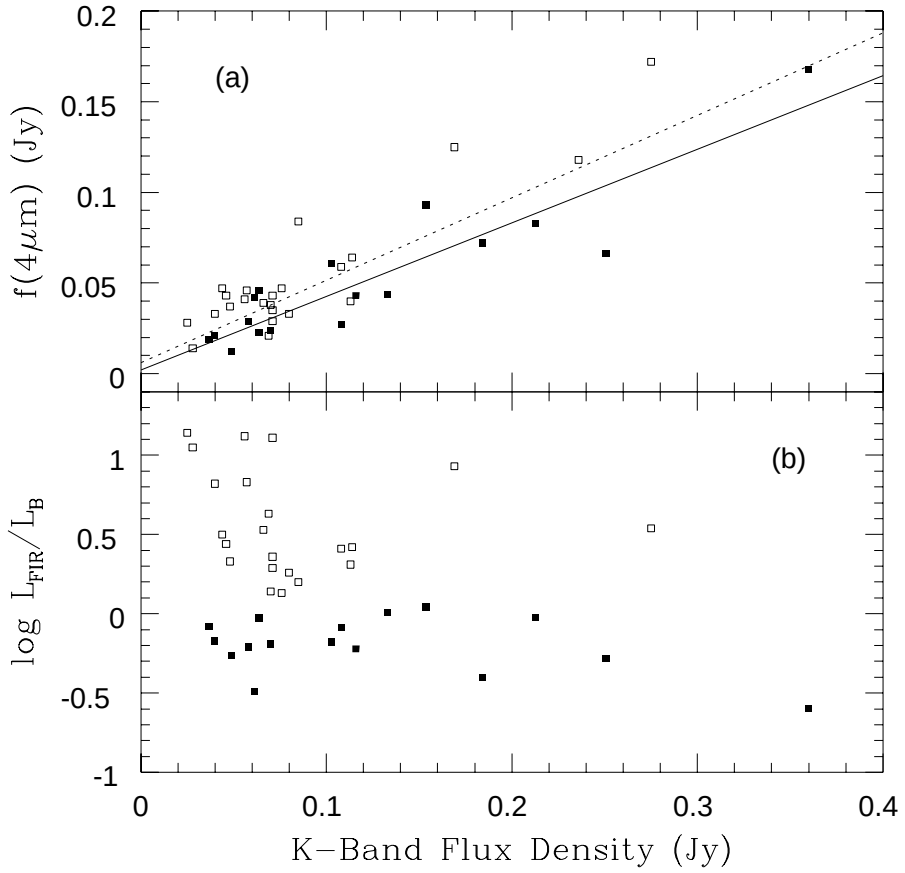

Fig. 12.— Plots of (a) the flux density at 4μm and (b) the FIR-to-blue luminosity ratio as a function of K-band flux density for 40 galaxies. The galaxies with $\log L_{\rm FIR}/L_{\rm B} < 0.1$ are represented by solid squares; notice that these galaxies have a flatter distribution in both plots, especially in (b), where they show no trend with increasing $\rm F_{\it K}$. The dotted line in (a) is a least-squares fit to all 40 galaxies, by minimizing their distances perpendicular to the fit. The solid line is a similar fit to the galaxies indicated by solid squares.